The dynamics of highly excited electronic systems: Applications of the electron force field

Julius T. Su and William A. Goddard III[a)]
Materials and Process Simulation Center, MC 139-74, Caltech, Pasadena, California 91125, USA

Highly excited heterogeneous complex materials are essential elements of important processes, ranging from inertial confinement fusion to semiconductor device fabrication. Understanding the dynamics of these systems has been challenging because of the difficulty in extracting mechanistic information from either experiment or theory. We describe here the electron force field (eFF) approximation to quantum mechanics which provides a practical approach to simulating the dynamics of such systems. eFF includes all the normal electrostatic interactions between electrons and nuclei and the normal quantum mechanical description of kinetic energy for the electrons, but contains two severe approximations: first, the individual electrons are represented as floating Gaussian wave packets whose position and size respond instantaneously to various forces during the dynamics; and second, these wave packets are combined into a many-body wave function as a Hartree product without explicit antisymmetrization. The Pauli principle is accounted for by adding an extra spin-dependent term to the Hamiltonian. These approximations are a logical extension of existing approaches to simulate the dynamics of fermions, which we review. In this paper, we discuss the details of the equations of motion and potentials that form eFF, and evaluate the ability of eFF to describe ground-state systems containing covalent, ionic, multicenter, and/or metallic bonds. We also summarize two eFF calculations previously reported on electronically excited systems: (1) the thermodynamics of hydrogen compressed up to ten times liquid density and heated up to 200 000 K; and (2) the dynamics of Auger fragmentation in a diamond nanoparticle, where hundreds of electron volts of excitation energy are dissipated over tens of femtoseconds. These cases represent the first steps toward using eFF to model highly excited electronic processes in complex materials. © *2009 American Institute of Physics*. [doi:10.1063/1.3272671]

I. INTRODUCTION

We wish to understand the processes that occur when complex materials are subjected to extremes of temperature, pressure, or radiation, whether at the surface of a fuel pellet in a fusion reactor, the interior of a giant planet, or the outer layers of a semiconductor being etched by electrons and ions. These systems have features that make them challenging to model: they may be heterogeneous, with extended interfaces between phases and a reactive volume extending over tens of thousands of atoms; they may be far from equilibrium, so that regions with hundreds of electron volts of excitation might be separated from much colder regions by only one bond; and they may undergo complex chemical reactions over time, with rates dependent on the degree of electronic excitation.

Methods exist to simulate electron dynamics, but their regime of application clusters around two extremes: cold systems with few atoms or hot systems with many atoms. For example, quantum mechanics (QM) methods can simulate with high accuracy the dynamics of electronic states in equilibrium (thermal smearing of the density matrix[1]), or can be used to compute a spectrum of excited potentials on which nuclear curve-hopping dynamics can be executed.[2] The computation of nonadiabatic dynamics using time-dependent density functional theory (DFT) is feasible but quite expensive, limited to tens of atoms and short time scales [<1 ps (Refs. 3–5)]. At another extreme, particle methods can simulate plasmas with millions of electrons, but are limited in application to weakly coupled plasmas[6]—i.e., high temperatures and no chemistry.

The method presented here, electron force field (eFF), can be viewed as an approximation to QM (wave packet dynamics[7–9]) or as an elaboration of plasma methods [fermionic molecular dynamics (MD)[10–15]], combining the ability of electronic structure methods to describe atomic structure, bonding, and chemistry in materials, and of plasma methods to describe nonequilibrium dynamics of large systems with highly excited electrons. The practicality of eFF relies on a drastic simplification of the electronic wave function.

- The electrons are described as floating Gaussian wave packets whose position and size respond instantaneously to the various forces during the dynamics.

- The wave function is taken to be a Hartree product of the wave packets. A spin-dependent Pauli potential is added to the Hamiltonian to compensate for the lack of explicit antisymmetry in the wave function.

a)Electronic mail: wag@wag.caltech.edu.

131, 244501-1

Just as conventional force fields average away electronic motions, to enable the simulation of nuclear dynamics on large scale (millions of atoms), eFF averages away fine details of electron structure and motion to enable the simulation of nuclear and electronic dynamics on a large scale (millions of electrons).

Substituting the eFF wave function into the time-dependent Schrodinger equation produces equations of motion that correspond—to second order—to classical Hamilton relations between electron position and size variables, and their conjugate momenta;[7] these equations can be integrated with conventional MD algorithms. Furthermore, the interactions between particles reduce to the sum of pairwise effective potentials—normal electrostatics between electrons and nuclei, a size-dependent kinetic energy for the electrons (exactly as in QM), and a spin-dependent Pauli potential—completing the analogy to conventional MD.

This paper is organized as follows. In Sec. II, we discuss the equations of motion and potentials that form eFF, with a particular focus on the functional form and parametrization of the Pauli potential, and on how the balance of interactions gives rise to stable atoms and bonds between atoms. We also discuss the algorithmic speedups that enable large scale calculations.

In Sec. III, we discuss ground-state systems, evaluating the ability of eFF to reproduce the geometries and energies of molecules containing covalent, ionic, multicenter, and/or metallic bonds, e.g., alkanes, both cyclic and acyclic; methyl radical, cation, and anion; allowed and forbidden reactions of hydrogen atoms and molecules; hydrides of lithium, beryllium, and boron; and lithium and beryllium metal, as well as the limiting case of a uniform electron gas. We make comparisons to DFT and other reference theories, as well as experiments, to judge the validity of the eFF potentials for describing different kinds of bonding.

In Sec. IV, we summarize calculations on two electronically excited systems, the results of which have been previously communicated.

(1) The thermodynamics and shock behavior of dense hydrogen, compressed up to ten times liquid density and heated up to 200 000 K.[16]

(2) The dynamics of Auger fragmentation in a diamond nanoparticle, where hundreds of electron volts of excitation energy are dissipated over tens of femtoseconds.[17]

These cases represent the first steps toward using eFF to model highly excited electronic processes in complex materials.

II. GENERAL THEORY OF THE eFF

A. Energy expression

The species in eFF are nuclei and electrons, where nuclei are point charges and electrons are floating spherical Gaussian wave functions ($\psi \propto \exp((\mathbf{r}-\mathbf{r_i})^2/s_i^2)$). The energy is then a function of the positions of the nuclei and electrons ($\mathbf{r}_i$), and also the sizes of the electrons (s_i). To compute ground states and adiabatic dynamics, the sizes and positions of the electrons are optimized—minimizing the overall energy—for each configuration of nuclear positions. To obtain excited state dynamics, a more complex form for the electron wave function and its associated equations of motion is needed; we present these in Sec. II B.

The task of computing the electronic energy is complicated by the fact that electrons are fermions. The simplest antisymmetric wave function, a Slater determinant, contains $N!$ product terms, and evaluating the energy of such a wave function requires N^4 operations, mostly in the computation of four-center electron-electron repulsion integrals. To avoid this prohibitive scaling, in eFF we compute instead the energy of the single-term Hartree product independent particle wave function, which requires only N^2 operations. We then add on a correction term evaluated as an N^2 pairwise sum between electrons that approximate the energy difference between the true antisymmetric wave function and the Hartree product wave function. Since the antisymmetry of the wave function is responsible for Pauli repulsion, this term can be called a "Pauli potential." This approach of adding Pauli repulsion as a correction makes eFF fast, so that it exhibits the computational cost of conventional MD rather than that of Hartree–Fock (HF) or density functional methods.

The Pauli pair potential in eFF is similar to those used in other fermionic MD methods.[10] Typically these potentials are formulated to exclude some region in phase space, so that fermions are well separated in position and momentum over a wide range of conditions. Pauli potentials have been employed to study nucleon collisions and reactions,[18] proton stopping by atomic targets,[19] and hydrogen plasma dissociation and ionization.[11,13]

However, existing Pauli pair potentials have been limited in accuracy and scope. For example, one potential used to describe hydrogen plasma[11] can compute interactions between electrons of different sizes (rather than assuming the electrons are all the same size)—essential for capturing changes in bonding during chemical reactions—yet it causes lithium hydride to be unbound and the valence electrons of alkanes to collapse onto their cores. Another potential[20] has been applied to create stable atoms with Z up to 94 (Ref. 21) which have a shell structure, but does not describe the structure of valence shells with enough accuracy to form reasonable bonds between atoms.

Our goal was to find a Pauli potential general in scope and accurate enough to describe energies and geometries of both ground states and highly excited states, while retaining sufficient simplicity to allow practical simulations of the electron dynamics of systems containing tens of thousands of atoms.

One approach to improve accuracy, although time consuming, is to compute the full antisymmetric energy of a Slater determinant of floating Gaussian orbitals; such a method is the basis of the floating spherical Gaussian orbital (FSGO) *ab initio* method pioneered by Frost in 1964.[22] The method produces good geometries for molecules such as lithium hydride, beryllium dihydride, first and second row hydrides, and hydrocarbons. Overall, eFF produces geometries as good or better than FSGO, but with much reduced computational expense.

The overall energy in eFF is a sum of a Hartree product kinetic energy, a Hartree product electrostatic energy, and an antisymmetrization (Pauli) correction,

$$E = E_{ke} + E_{nuc \cdot nuc} + E_{nuc \cdot elec} + E_{elec \cdot elec} + E_{Pauli}, \quad (1)$$

where the terms are defined as follows:

$$E_{ke} = \frac{\hbar^2}{m_e} \sum_i \frac{3}{2} \frac{1}{s_i^2}, \quad (2a)$$

$$E_{nuc \cdot nuc} = \frac{1}{4\pi\epsilon_0} \sum_{i<j} \frac{Z_i Z_j}{R_{ij}}, \quad (2b)$$

$$E_{nuc(i) \cdot elec(j)} = -\frac{1}{4\pi\epsilon_0} \sum_{i,j} \frac{Z_i}{R_{ij}} \mathrm{erf}\left(\frac{\sqrt{2}R_{ij}}{s_j}\right), \quad (2c)$$

$$E_{elec(i) \cdot elec(j)} = \frac{1}{4\pi\epsilon_0} \sum_{i<j} \frac{1}{r_{ij}} \mathrm{erf}\left(\frac{\sqrt{2}r_{ij}}{\sqrt{s_i^2 + s_j^2}}\right), \quad (2d)$$

$$E_{Pauli} = \sum_{\sigma_i = \sigma_j} E(\uparrow\uparrow)_{ij} + \sum_{\sigma_i \neq \sigma_j} E(\uparrow\downarrow)_{ij}, \quad (2e)$$

where s_i are the sizes of the electrons, σ_i are the (fixed) spins of the electrons, Z_i are the charges on the nuclei, R_{ij} are the distances between the nuclei in Eq. (2b) and between the nuclei and electrons in Eq. (2c), and r_{ij} are the distances between electrons.

The potentials $E_{nuc \cdot nuc}$, $E_{nuc \cdot elec}$, and $E_{elec \cdot elec}$ in Eqs. (2b)–(2d) are simply the electrostatic energy between a set of delocalized charges, and would not be out of place in a classical force field. On the other hand, the potentials E_{ke} and E_{Pauli} in Eqs. (2a) and (2e) represent quantum mechanical effects, as suggested by the presence of both the electron mass m_e and Planck's constant $\hbar$. Typically we use atomic units, setting $m_e = 1$, $\hbar = 1$, and $1/(4\pi\epsilon_0) = 1$.

The Pauli potential E_{Pauli} is the sum of spin-dependent terms $E(\uparrow\uparrow)$ and $E(\uparrow\downarrow)$, which act between same spin and opposite spin pairs of electrons, respectively, and are defined as follows:

$$E(\uparrow\uparrow)_{ij} = \left(\frac{S_{ij}^2}{1 - S_{ij}^2} + (1-\rho)\frac{S_{ij}^2}{1 + S_{ij}^2}\right)\Delta T_{ij}, \quad (3a)$$

$$E(\uparrow\downarrow)_{ij} = \frac{\rho S_{ij}^2}{1 + S_{ij}^2}\Delta T_{ij}, \quad (3b)$$

where ΔT is a measure of the kinetic energy change upon antisymmetrization and S is the overlap between two wave packets,

$$\Delta T_{ij} = \frac{\hbar^2}{m_e}\left(\frac{3}{2}\left(\frac{1}{\bar{s}_1^2} + \frac{1}{\bar{s}_2^2}\right) - \frac{2(3(\bar{s}_1^2 + \bar{s}_2^2) - 2\bar{r}_{12}^2)}{(\bar{s}_1^2 + \bar{s}_2^2)^2}\right), \quad (4)$$

$$S_{ij} = \left(\frac{2}{\bar{s}_i/\bar{s}_j + \bar{s}_j/\bar{s}_i}\right)^{3/2} \exp(-\bar{r}_{ij}^2/(\bar{s}_i^2 + \bar{s}_j^2)), \quad (5)$$

where $\rho = -0.2$, $\bar{x}_{ij} = x_{ij} \cdot 1.125$, and $\bar{s}_i = s_i \cdot 0.9$, corresponding to the three universal parameters in the force field.

Section II C explains the consequences of the combined kinetic energy and electrostatics terms for chemical bonding, and Sec. II D provides further motivation for the Pauli expression above. Further details of the derivation of the energy expressions are provided in the supporting information.[23]

B. Time evolution and equations of motion

To simulate materials at finite temperatures, we propagate semiclassical electron dynamics,[7,13] allowing the positions of the nuclei and electrons, as well as the sizes of the electrons, to change over time. In this formulation, nuclei are point particles and electrons are spherical Gaussian wave packets, termed "thawed" functions by Heller,[7]

$$\Psi(\mathbf{r}) \propto \exp\left[-\left(\frac{1}{s^2} - \frac{2p_s}{s}\frac{i}{\hbar}\right)(\mathbf{r} - \mathbf{x})^2\right]\exp\left[\frac{i}{\hbar}\mathbf{p_x} \cdot \mathbf{r}\right]. \quad (6)$$

In the above expression, $\mathbf{x}$ and s are the position and size of the wave packet, while $\mathbf{p_x}$ and p_s are the corresponding conjugate momenta, representing the translational motion and radial expansion/shrinking of the wave packet over time. Substituting the wave function into the time-dependent Schrodinger equation and assuming a locally harmonic potential produces the semiclassical equations of motion,

$$\dot{\mathbf{p}}_\mathbf{x} = -\nabla_x V, \quad (7a)$$

$$\dot{\mathbf{x}} = m_e^{-1}\mathbf{p_x}, \quad (7b)$$

$$\dot{p}_s = -\partial V/\partial s, \quad (7c)$$

$$\dot{s} = (3m_e/4)^{-1}p_s. \quad (7d)$$

The radial mass factor $3m_e/4$ in Eq. (7d) depends on the dimensionality of the wave packet, and becomes $2m_e/4$ for a two-dimensional wave packet and $m_e/4$ for a one-dimensional wave packet. Overall, the average position of the wave packet obeys classical dynamics (Ehrenfest's theorem) with the addition that the size of the wave packet obeys classical dynamics as well.

The kinetic energy of the wave packet separates into two components, one related to the spatial oscillations of the wave function, determined by the translational and radial momenta, and the other related to the envelope of the wave function, determined by the size s. We call the first component a *kinetic energy of motion*,

$$T = \sum_i \frac{1}{2}m_e|\dot{\mathbf{x}_i}|^2 + \frac{1}{2}\left(\frac{3}{4}m_e\right)\dot{s}_i^2, \quad (8)$$

and call the second component an *electronic kinetic energy*,

$$E_{ke} = \frac{\hbar^2}{m_e}\frac{3}{2}\frac{1}{s_i^2}, \quad (9)$$

which is identical to the kinetic energy of a stationary Gaussian wave function, as defined in Eq. (2a). To permit a closer analogy to classical force fields, we include the electronic kinetic energy as part of the potential energy V of the system, since it is nonzero even when the wave packet is stationary.

The two components of kinetic energy can interconvert—as an example, a localized electron in free space expands radially outward over time, transforming its electronic kinetic energy into a kinetic energy of motion. The total energy $T+V$ is a constant of motion.

The mass of the electron m_e appears in three places: first, in the electronic kinetic energy (2a); second, in the Pauli energy (2e); and third, in the equations of motion (7a). We now consider the effect of modifying m_e in these three locations. In the first two cases, changing m_e affects the sizes of electrons in atoms, and the lengths of bonds in molecules—hence, we always keep m_e in Eqs. (2a) and (2e) fixed, so as to not disrupt the chemistry of the system. On the other hand, changing m_e in Eq. (7a) has the more subtle effect of varying the overall time scale of excited electron motions, with the time scale of excitation relaxations and energy transfer proportional to $m_e^{1/2}$. In some cases, it is useful to modify m_e in Eq. (7a) while leaving m_e in Eqs. (2a) and (2e) fixed; we refer to this operation as changing the *dynamic* masses of the electrons.

There were two situations where changing the dynamic masses of the electrons proved useful. The first situation arose in simulating adiabatic dynamics, where the forces were determined from the wave function, as in Car–Parrinello molecular dynamics, where the mass of the electron is typically taken to be ~500 a.u. The second situation arose in simulating the dynamics of the Auger process (Sec. IV B); in that sequence of events, the dynamics of the electrons is dominated by a single characteristic time scale, and eFF shortens the time scale by roughly a factor of 40, essentially because the localized nature of the eFF wave function allows too fast relaxation (low electronic friction). In that case, we found that a dynamic mass of ~1836 a.u. led to the same time scale as experiment.

C. Bonding comes from balancing kinetic energy and electrostatics

Atoms have finite size, and bonds finite extent, because kinetic energy pressure and electrostatics exert opposing forces on the sizes of electrons. As an example, consider a hydrogenic atom with a nucleus of charge Z and an electron, where the electron wave function is defined as a single Gaussian function of size s. As we vary s, the kinetic energy changes as $\int |\nabla \phi|^2 dV \propto (1/s)^2$, while the potential energy changes as $-1/s$. With the constants of proportionality included, and using atomic units, the total energy is

$$E = \frac{3}{2}\frac{1}{s^2} - \sqrt{\frac{8}{\pi}}\frac{Z}{s}. \qquad (10)$$

The physical interpretation of the two terms is as follows: electrostatics attempts to squeeze the electron into a point on top of the nucleus, while kinetic energy pressure prevents this collapse, as implied by Heisenberg's uncertainty principle. The balance of the two radial forces creates an atom with a stationary size of $s = (3/2\sqrt{\pi/2})Z^{-1} \approx 1.88Z^{-1}$ bohr, and $E = -(4/3\pi)Z^2 \approx -0.424 \times Z^2$ hartree.

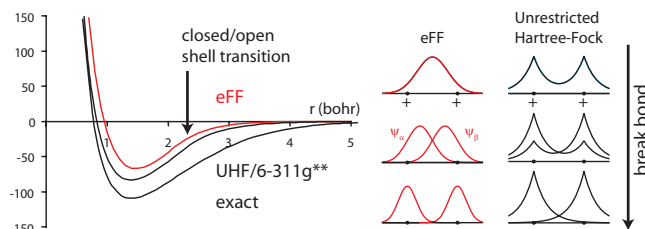The hydrogenic atom energy is ~15% above the exact value of $E = -(1/2)Z^2$ hartree because a single Gaussian

FIG. 1. H_2 potential energy surface (kcal/mol); eFF properly dissociates H_2, but the simplicity of the basis, as well as the neglect of electron correlation, leads to underbinding.

function does not have a sharp cusp at the nucleus (needed to cancel to Coulomb singularity), and it also falls off too quickly at large distances. However, since most applications involve energy differences between states containing the same core electrons, and with atoms in moderate to close proximity to each other, there errors cancel to a large degree.

The extent and polarity of covalent bonds are also governed by a balance of kinetic energy and electrostatics. In molecules the eFF bonding electrons are shifted away from the nuclear centers to lie between multiple nuclei, with the precise position reflecting the relative electronegativities of the atoms. Thus in H_2, the two eFF orbitals sit at the midpoint of the nuclei. The electrons shrink to interact more strongly with both protons ($s=1.77$ bohr versus 1.88 bohr in the atoms), and the decreased potential energy of having each electron interact with two protons instead of one makes the bond stable (Fig. 1).

Pulling the protons apart decreases the mutual attraction of electrons and nuclei, and weakens the bond. As the length of the bond is increased past 2.1 bohr, it becomes favorable for the electrons to become centered on the nuclei. The energy varies smoothly as the different spin electrons separate, breaking symmetry, and the wave function goes from a closed shell to an open shell form. In HF theory, the analogous transition between restricted and unrestricted wave functions occurs at 2.3 bohr. Comparing eFF with exact values, we find that the optimum bond length is nearly correct (1.47 Å eFF versus 1.40 Å exact[24] and 1.38 Å for HF), while the binding energy is underestimated (67 kcal/mol eFF versus 109 kcal/mol exact and 86 kcal/mol for HF).

There are several reasons for the energy discrepancy. In H_2 molecule, the true electron density is doubly peaked, reaching a maximum at the nuclear centers. Because the single Gaussian wave function cannot become multiply peaked, the bond energy is underestimated. Also, a measure of static correlation is missing in both eFF and HF due to the single configuration nature of the underlying wave functions; as made explicit in valence bond (VB) or generalized valence bond (GVB) descriptions, in H_2 there is a resonance stabilization between having the spin up electron on the right and the spin down electron on the left, and vice versa. The neglect of this resonance in eFF and HF makes the energy fall to zero too quickly as the bond is stretched. Finally, the dynamic correlation of the two electrons of H_2 instantaneously avoiding each other to reduce their mutual repulsion is missing. This correlation effect stabilizes H_2 molecule relative to H atoms, and its neglect contributes to the H_2 underbinding.

Issues of underbinding aside, the floating Gaussian description of electrons gives a potential energy curve for hydrogen molecule dissociation that has a proper inner wall, bonding region, long range tail, and a correct transition between closed and open shell wave functions.

D. Pauli principle causes same spin electrons to repel; a parametrization

The Pauli principle effectively forces same spin orbitals on neighboring atoms to be orthogonal to each other;[25] we review this interpretation below. When a system is compressed, this orthogonality effect causes the kinetic energy of the orbitals to increase dramatically as the electrons are squeezed together.[26] This repulsive force is the dominant interaction between neutral molecules at short range—it is the basis of the steric effect in chemistry, it prevents stars from collapsing, and it prevents the reader from falling through the Earth. Within molecules, the Pauli principle drives core and valence electrons into separate shells, and controls the hybridization of electron around atoms, and hence the bonding between atoms. Thus an accurate description of the Pauli principle is a key; yet it is potentially the most time-consuming energy contribution to compute.

The Pauli potential is defined as the difference in energy between a Slater determinant of orbitals and a Hartree product of the same orbitals,

$$E_{\text{Pauli}}[\{\phi_i\}] = E(\mathcal{A}(\phi_1 \cdots \phi_N)) - E(\phi_1 \cdots \phi_N), \tag{11}$$

where ϕ_i are the orbitals and $\mathcal{A}$ is the antisymmetrizer. This energy difference is also termed the *exchange energy* of the system.

Consider the kinetic energy contribution to E_{Pauli}, where the kinetic energy of a wave function Ψ is given by $\text{KE}(\Psi) = \langle \Psi | -\frac{1}{2}\nabla^2 | \Psi \rangle$. For a Hartree product,

$$\text{KE}(\phi_1 \cdots \phi_N) = \text{KE}(\phi_1) + \cdots + \text{KE}(\phi_N), \tag{12}$$

while for a Slater determinant,

$$\text{KE}(\mathcal{A}(\phi_1 \cdots \phi_N)) = \text{KE}(\mathcal{A}(\chi_1 \cdots \chi_N))$$
$$= \text{KE}(\chi_1) + \cdots + \text{KE}(\chi_N), \tag{13}$$

where $\{\chi_i\}$ are orthogonal orbitals, related to $\{\phi_i\}$ through a matrix $\mathbf{U}$ (many are possible),

$$\chi_i = \sum_j U_{ij}\phi_j. \tag{14}$$

Since χ are linear combinations of ϕ, the determinant is unaffected, and since $\langle \chi_i | \chi_j \rangle = \delta_{ij}$, cross terms in the kinetic energy expression (13) vanish, making the above separation of terms possible. Hence the kinetic energy portion of the Pauli energy is simply

$$\Delta\text{KE} = \sum_i \text{KE}(\chi_i) - \text{KE}(\psi_i), \tag{15}$$

which is commonly called an "orthogonalization energy."

When two nodeless orbitals approach each other, the expression (15) produces a Pauli *repulsion*. To understand why, consider two orbitals ϕ_1 and ϕ_2 and their orthogonalized counterparts,
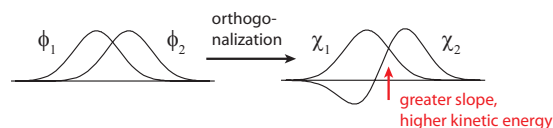

FIG. 2. Pauli repulsion comes from the kinetic energy increase upon making orbitals orthogonal to each other. This effect increases with the overlap between orbitals, and is the dominant contribution to the Pauli energy when the interacting electrons are nodeless and spherical.

$$\chi_1 = \phi_1, \tag{16}$$

$$\chi_2 = \phi_2 - S_{12}\phi_1, \tag{17}$$

where $S_{12} = \langle \phi_1 | \phi_2 \rangle$ is the overlap between the orbitals. Figure 2 shows that as the overlap increases, the slope of ϕ_2 in the interaction region increases sharply, leading to an increase in kinetic energy, which translates into a repulsive force.

Kinetic energy difference-based Pauli potentials have been obtained and used by Boal and Glosli,[27] who considered the case of same size nucleons; and by Klakow,[11] who considered the more general case of Pauli repulsion between different size electrons. The forms of these potentials bear some resemblance to earlier Pauli potentials for nucleons[28,29] that decay as e^{-ax^n}, where x is the distance between electron centers and a and n are arbitrary parameters.

When the electrons involved are nearly spherical and nodeless, the kinetic energy effects described above account for the majority of the Pauli interaction, and we approximate the Pauli energy by the kinetic energy contribution alone. This is a reasonable description of the electrons in many systems with low nuclear charge ($Z=1-6$); lithium hydride, for example, has s-like electrons shifted slightly away from the nuclei, befitting its ionic nature, while methane can be described in terms of four localized and covalent bonds.

This approximation breaks down when electrons have substantial density on both sides of the nucleus, as in the lone pairs of neon, the π bond of ethylene, or the unpaired electron of methyl radical. In those cases, the p electrons are already orthogonal to each other, their overlap is zero, and the kinetic energy contribution to the Pauli interaction becomes zero. Other terms then dominate, and a more complex Pauli potential is needed; this will be the subject of a future paper. For the purpose of this article, we restrict ourselves to systems where electrons are s-like, or contain p character only insofar as a single lobe of electron density is shifted away from the nuclear center.

In deriving the Pauli potential of eFF, we assume that kinetic energy effects dominate and add in a pairwise fashion. For a pair of same spin electrons, the Hartree product wave function is $\Psi = \phi_1(r_1)\phi_2(r_2)$, while the Slater determinant wave function is

$$\Psi' = \frac{1}{\sqrt{2-2S^2}}(\phi_1(r_1)\phi_2(r_2) - \phi_2(r_1)\phi_1(r_2)), \tag{18}$$

where the factor containing $S = \int \phi_1\phi_2 dV$ ensures that the wave function is normalized. Then we estimate the Pauli energy between wave functions ϕ_1 and ϕ_2 as the kinetic energy difference
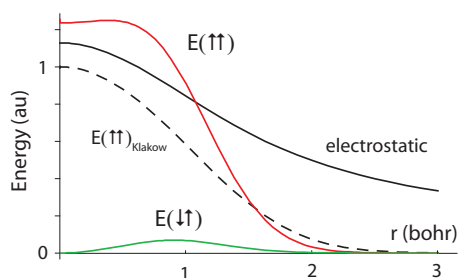
FIG. 3. Comparison of Pauli repulsion and electrostatic repulsion between two wave functions with $s=1$. The Pauli repulsion rises more sharply with increasing electron overlap than electrostatic repulsion, acting almost as a hard-sphere potential. This behavior gives rise to the basic rules of Lewis bonding and hybridization, which we discuss in greater depth in Sec. III B.

$$E_u = \langle \Psi' | -\tfrac{1}{2}\nabla^2 | \Psi' \rangle - \langle \Psi | -\tfrac{1}{2}\nabla^2 | \Psi \rangle, \tag{19}$$

$$= \frac{S^2}{1-S^2}\left(t_{11} + t_{22} - \frac{2t_{12}}{S} \right), \tag{20}$$

where $t_{ij} = \langle \psi_i | -\tfrac{1}{2}\nabla^2 | \psi_j \rangle$ [detailed derivation given in supporting information S1 (Ref. 23)].

The Pauli potential due to Klakow[11] uses $E(\uparrow\uparrow) = E_u$ and $E(\uparrow\downarrow) = 0$. To obtain our expression, we use VB wave function

$$\Psi_{VB} = \frac{1}{\sqrt{2+2S^2}}(\phi_1(r_1)\phi_2(r_2) + \phi_2(r_1)\phi_1(r_2)). \tag{21}$$

Then we compute

$$E_g = \langle \Psi_{VB} | -\tfrac{1}{2}\nabla^2 | \Psi_{VB} \rangle - \langle \Psi | -\tfrac{1}{2}\nabla^2 | \Psi \rangle, \tag{22}$$

$$= \frac{S^2}{1+S^2}\left(t_{11} + t_{22} - \frac{2t_{12}}{S} \right), \tag{23}$$

which can be considered a static correlation energy. We mix E_g and E_u together, and scale the electron sizes and distance between electrons by a set of fixed and universal parameters $\bar{s}/s$ and $\bar{r}/r$, whose values are given below. Finally we calculate the functions

$$E(\uparrow\uparrow) = E_u - (1+\rho)E_g,$$

$$E(\uparrow\downarrow) = \rho E_g,$$

which include a mixing parameter ρ. Figure 3 shows that the effect of the E_g term is to make the Pauli potential between both opposite and same spin electrons more repulsive; this reduces the known tendency for floating orbitals to coalesce into each other and become linearly dependent.

The parameter ρ and the scaling factors $\alpha = \bar{s}/s$ and $\beta = \bar{r}/r$ were fixed to produce correct geometries for a range of test structures such as LiH, CH_4, and C_2H_6 and B_2H_6. Their values are

$$\alpha = \bar{s}/s = 0.9,$$

$$\beta = \bar{r}/r = 1.125,$$

$$\rho = -0.2.$$

These Pauli parameters are universal—they are not adjusted further in any of the ground state or electronically excited systems studied below.

E. Evaluation of long range forces

In traditional MD, cutoffs are often used to minimize the number of pairwise interactions that must be considered. Electrostatic interactions pose a particular challenge, as they decay slowly ($\sim 1/r$), and in small periodic systems, multiple charge replicas must be considered. Typically, methods such as particle-mesh Ewald or multigrid solutions to Poisson's equation are used to efficiently evaluate the contribution from long-range electrostatics. In principle, such schemes could be applied to compute eFF energies as well. Instead, we have chosen to implement two simpler methods, one suited for the computation of small periodic systems ($L < 50$ bohr), and the other suited for the computation of all other system types.

The first approach is an Ewald method generalized to Gaussian charge densities. We define a threshold charge width $s_{threshold} = 3.54$ bohr. Charges with $s < s_{threshold}$ are summed over real space with multiple replicas, while charges with a larger width are summed over reciprocal space, leaving an equal and opposite combination of charges to be summed over real space. More details are provided in the Appendix.

The second approach multiplies an absolute cutoff function to the electron-electron, electron-nuclear, and Pauli pairwise interactions. A similar scheme to replace long-range electrostatic interactions with shorter-range potentials has been proposed recently.[30] The cutoff function used here is a seventh order spline that goes from 1 to 0 over the radial distance range $r_{cutoff} = 0-20$ bohr, and is defined so that the first, second, and third derivatives at the end points are zero; the expression is

$$f_{cutoff} = 20x^7 - 70x^6 + 84x^5 - 35x^4 + 1, \tag{24}$$

where $x = r/r_{cutoff}$. By multiplying a cutoff function over such an extended range, we avoid artifacts due to sharp changes in forces or energies over short distances. Also, by restricting the application of this method to large unit cells, we enable the use of the minimum-image convention, which greatly accelerates the computation of periodic electrostatics. In tests on nonperiodic lithium solids (cohesive energy of ~ 60 kcal/mol/atom), a cutoff of 20 bohr resulted in an error of 2.1 kcal/mol/atom, while a larger cutoff of 50 bohr resulted in an error of only 0.06 kcal/mol/atom.

When the second approach is used, we divide the simulation space into bins that are the size of the cutoff length, and only evaluate interactions inside bins and between nearest neighbor bins. This results in a linear-scaling algorithm that makes computations with millions of electrons feasible (Fig. 4).
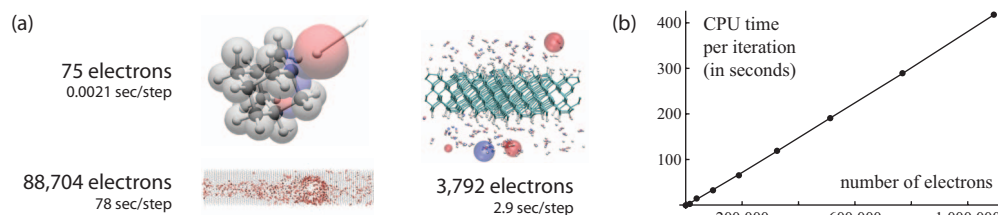
FIG. 4. (a) Timings on a 2.33 GHz Xeon for the Auger fragmentation of $C_{10}H_{16}$, plasma etching of a diamond surface, and proton stopping in beryllium. (b) Linear scaling of calculation time using a 10 Å force cutoff; shown is the time spent on an energy/force evaluation on bulk lithium solid. The memory required also scales linearly with the number of electrons and nuclei.

III. RESULTS FOR GROUND STATE SYSTEMS

A. Reference calculations

For the sake of consistency, we compare relative energies and geometries of ground state systems with a single reference level of theory, density functional theory in the form of unrestricted B3LYP/6-311g**,[31] which we abbreviate as DFT for the remainder of the paper. In situations where DFT may be less accurate, e.g., investigating the reaction of H_2 with H atom and the stability of methyl carbanion, we have included the results of high level *ab initio* calculations from the literature as well. In cases where there is a great difference between eFF and DFT, we have also included the results of HF (HF/6-311g**) computations to judge the magnitude of the error that may have been incurred by not explicitly including the effects of electron correlation.

B. Tetrahedral carbon forms bonds to other carbons and hydrogen

In atoms and molecules optimized with eFF, we observe (1) pairing of opposite spin electrons into the same spatial orbital (2) separation of electrons into nucleus-centered core electrons and nucleus-distant valence electrons (for $Z>2$) and (3) nearest-neighbor packing of valence electrons into configurations with a maximum of four electron pairs around each core ("octet rule"). These basic rules of Lewis bonding and hybridization arise as a natural result of minimizing the sum of electrostatic potential, kinetic energy pressure, and Pauli repulsion.

For example, in saturated hydrocarbons, the eFF valence electrons properly arrange themselves into a tetrahedral sp^3 packing (Fig. 5). In methane, the eFF valence electrons sit between the carbon and hydrogen nuclei, but at ~80% of the distance from the core center to the proton, reflecting the greater electronegativity of carbon versus hydrogen. In ethane, by contrast, the carbon-carbon bonding electrons are centered exactly halfway between the two nuclei, since the two atoms have equal electronegativity.

eFF properly finds that C–C bonds are longer than C–H bonds (Table I), which are in turn longer than the H–H bond (0.75 Å). This difference in bond lengths arises as a consequence of Pauli repulsion between the electrons of the sigma bond and the electrons of the $1s^2$ core of a carbon atom. The correct ordering of bond lengths persists and occurs over a wide range of Pauli parameters, but to obtain the precise C–C and C–H bond distances requires that the Pauli parameters α and β be fine tuned (Sec. II D).

There are some deviations in bond angles and in C–H bond lengths for highly substituted carbons, which arise because C–C bonding electrons in eFF are too small and centralized, causing them to repel each other too much (Table I), pushing together and lengthening the C–H bonds. For example, isobutane ($CH(CH_3)_3$) has a too-small HCC angle (101.8° instead of 109.4° DFT) and a too-long carbon-hydrogen bond length (1.42 Å versus 1.10 Å DFT). There is a cancellation of errors, though, which causes the variations in C–H bond energies to be modest, as shown in Sec. III F. Also, carbon-carbon bond lengths are relatively independent of substitution, as they should be.

Figure 6 shows that eFF can describe a variety of bridged, fused-cyclic, and strained carbon skeletons with largely correct carbon-carbon distances. The exception is compounds containing quaternary carbons, which have C–C bonds that are too long, due to the too-strong repulsion of C–C bonds outlined above. For example, ^tBu-^tBu has a C–C
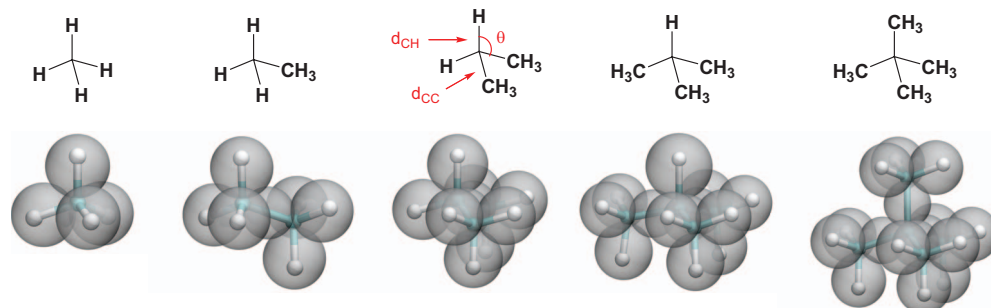

FIG. 5. eFF geometries of simple substituted hydrocarbons. The valence electrons spin pair into matching spatial orbitals, shown here as gray spheres. The basic rules of Lewis bonding and hybridization arise as a natural result of minimizing the sum of electrostatic potential, kinetic energy pressure, and Pauli repulsion. Geometries are in Table I.

TABLE I. Geometries of primary, secondary, and tertiary-substituted carbon. The deviations highlighted in boldface are caused by a too-strong repulsion between C–C bonding electrons.

	d_{CC} (Å)		d_{CH} (Å)		θ_{HCH} (deg)	
	eFF	DFT	eFF	DFT	eFF	DFT
CH_4			1.143	1.091		
$CH_3(CH_3)$	1.501	1.531	1.173	1.093	110.8	111.3
$CH_2(CH_3)_2$	1.513	1.532	**1.229**	1.095	107.9	109.4
$CH(CH_3)_3$	1.529	1.534	**1.424**	1.098	**101.8**	107.8
$C(CH_3)_4$	1.573	1.540				

bond length of 1.71 Å versus 1.59 Å DFT, and diamond has a C–C bond length of 1.68 Å versus 1.55 Å DFT.[32]

C. Carbon can form multiple bonds of the σ-π type, but poorly

When two electron pairs are squeezed into the space between the carbon nuclei of ethylene, they may avoid each other by forming "banana bonds" (electron pairs above and below the plane), or by forming σ-π bonds. In the HF description, the two pictures are equivalent because of the invariance of the antisymmetrized product to unitary transformations.

In eFF, there is no mixing of orbitals, and we expected banana bonding might be preferred, since no provision had been made for electrons to attain p character. Another possibility, observed previously in FSGO calculations,[33] is that the two electron pairs might draw arbitrarily close together to form a p function when antisymmetrized,
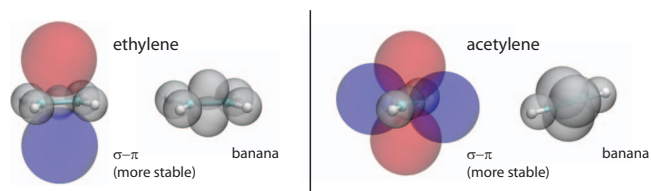

FIG. 7. Multiple bonds can split σ-π or form symmetric "banana" pairs. In eFF, σ-π bonding is strongly preferred, but the resulting p-like function is polarized and too diffuse, and incapable of providing substantive additional bonding strength.

$$e^{-\alpha(x+\Delta/2)^2} - e^{-\alpha(x-\Delta/2)^2} \rightarrow -2axe^{-ax^2}, \quad (25)$$

as $\Delta \rightarrow 0$. The coalescence of orbitals in this fashion is problematic, as it creates a negligible barrier to rotation about the π bond of ethylene, which is unphysical. It also results in a linearly dependent set of functions, which can cause numerical difficulties.

Neither of these outcomes is observed with eFF. There is no catastrophic coalescence of orbitals and no banana bonds. Indeed, contrary to our expectations, eFF prefers σ-π bonding. But it achieves this bonding in a curious way: a sigma electron pair sits in between the carbons, then the electrons of the other electron pair split, so that an electron of one spin sits above the plane, and an electron of the other spin sits below the plane (Fig. 7). This spin-polarized bond creates a diffuse p-like function; this mode of sigma-pi bonding is stabilized over equivalent banana bonding in eFF by a colossal 160 kcal/mol for double bonds and 183 kcal/mol for triple bonds.

The p-like functions thus created in eFF are too diffuse in the region above and below the plane, which causes inap-
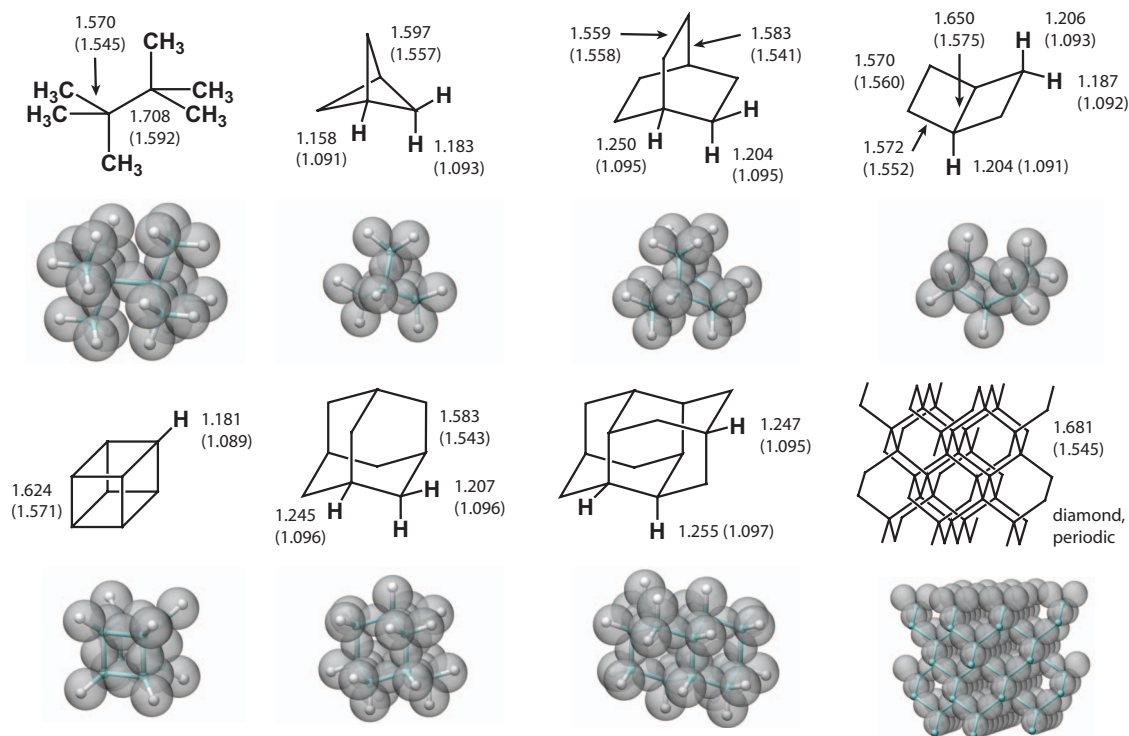

FIG. 6. eFF geometries of larger hydrocarbons. Bond lengths are in angstrom, and DFT values are given in parentheses for comparison. Overall, the bond lengths and angles of the carbon-carbon framework are correct, although carbon-carbon bonds attached to quaternary carbons are uniformly too long.

TABLE II. Geometries of double and triple bonds with bond lengths in angstrom.

		Ethylene	Acetylene
d_{CC}	eFF-$\sigma\pi$	1.517	1.383
	eFF-banana	1.442	1.334
	DFT	1.327	1.198
d_{CH}	eFF-$\sigma\pi$	1.089	1.052
	eFF-banana	1.125	1.064
	DFT	1.086	1.063

propriate steric clashes with any elements approaching above and below the π bond. They also do not contribute much to the overall strength of the bond: the multiple bonds in ethylene and acetylene are too long (Table II) and far too readily hydrogenated (for ethylene, $\Delta E_{hydrogenation}$ is -142 kcal/mol versus -39 kcal/mol DFT, and for acetylene, -407 versus -50 kcal/mol DFT).

In short, the current eFF does not properly describe multiple bonds, which arises as a corollary of a more general inability to describe electrons that have substantial p character, especially when electron density is expected to be present on both sides of the nucleus. In its present form, eFF should be used to model systems containing sigma-type electrons only.

D. Conformational analysis of alkanes proves quite accurate

Hydrocarbons often exist in a variety of stable conformations that differ by the extent of torsional rotation about carbon-carbon single bonds in the molecule. We now consider whether eFF can accurately reproduce the geometries and relative energies of these different conformations.

Figure 8 shows a series of cyclic hydrocarbons optimized with eFF. In the smallest molecule, cyclopropane, the carbon-carbon bonds are known to be curved, a compromise between the geometrical requirements of the molecule (60°) and the hybridization of orbitals on carbon (109.5°). According to eFF, the bonding electrons lie outside the perimeter of a line drawn connecting the carbons, with an angle between
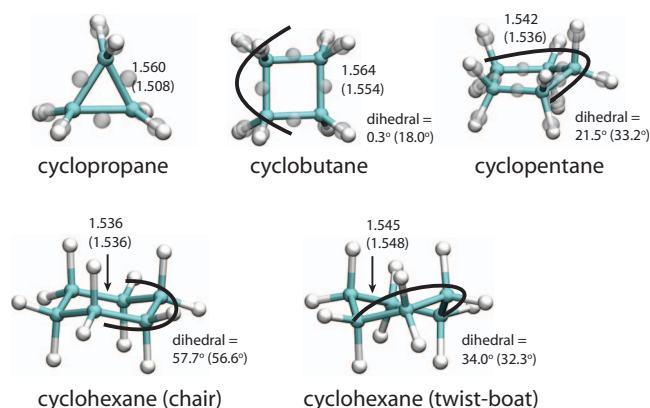

FIG. 8. Geometry optimization of a series of cyclic hydrocarbons. eFF reproduces the curved bonds of cyclopropane and the puckered (nonplanar) geometry of cyclopentane and cyclohexane; it also reproduces the energy difference between twist boat and chair conformations of cyclohexane.

TABLE III. Energy differences between conformers examined. Overall, the agreement between eFF and DFT is excellent.

System	Energy of	Relative to	ΔE (kcal/mol) eFF	ΔE (kcal/mol) DFT
Ethane	Eclipsed	Staggered	2.1	2.7
Butane	Gauche	*trans*	1.6[a]	0.9
Cyclohexane	Twist-boat	Chair	4.7	6.3
1,3-dimet.-cyclhex.	Ax-ax	Eq-eq	5.8	5.9
	Ax-eq	Eq-eq	2.7	2.1
Decalin	*cis*	*trans*	12.1	3.2
2-pentene	Major	Minor	5.5	4.6

[a]Gauche butane is not a local minimum and is constrained at 60°.

bonding electrons of 98°; GVB calculations[34] show similarly curved bonds with an interorbital angle of 110°. Curved bonds appear naturally in eFF as a consequence of the repulsion between the three carbon-carbon bonding electron pairs.

Proceeding to larger rings, it is known that cyclobutane and cyclopentane "pucker," placing atoms out of plane so that the orbitals on each atom can relax to their preferred tetrahedral configuration. eFF reproduces this pucker in cyclopentane (dihedral 21.5° versus 33.2° DFT) but not in cyclobutane (dihedral 0.3° versus 18.0° DFT)—this may be acceptable, given that the energy difference between puckered and planar cyclobutane is known to be small ($\sim$1.5 kcal/mol DFT).

In cyclohexane, there are two conformers—chair and twist boat—with a more substantial energy difference of 6.3 kcal/mol (DFT, Table III). eFF obtains an energy difference of 4.7 kcal/mol and dihedral angles that compare well to known values (57.7° versus 56.6° DFT for the chair and 34.0° versus 32.3° DFT for the twist-boat). The agreement of cyclohexane energies and geometries with B3LYP values is remarkable, considering that it involves a balance between the torsional barriers of rotation about carbon-carbon bonds and steric repulsions between axial hydrogens. To test whether the agreement is fortuitous, or the result of summing accurately computed quantities, we examine the conformational preferences of some simpler systems (Fig. 9 and Table III).

In ethane, the energy difference between eclipsed and staggered conformations—known to be a consequence of Pauli repulsion between C–H bond electrons—is slightly too low (2.1 versus 2.7 kcal/mol DFT). In butane, we find the difference between *gauche* and *trans* forms, which arises from the repulsion between methyl groups, to be slightly too high (1.6 versus 0.9 kcal/mol DFT). This difference is not surprising given our previous observation that carbon-carbon bonds repel carbon-hydrogen bonds more than they should. The combination of large methyl-methyl repulsions and small barriers for hydrogen eclipsing causes the energy barrier between *gauche* and *trans* butane to improperly vanish.

In substituted cyclohexanes, axial substituents can become equatorial through a "chair flip." The stability of a cyclohexane conformer is particularly affected by repulsions between axial substituents, since they are close to each other (2.66 Å DFT) and oriented in the same direction. To quantify
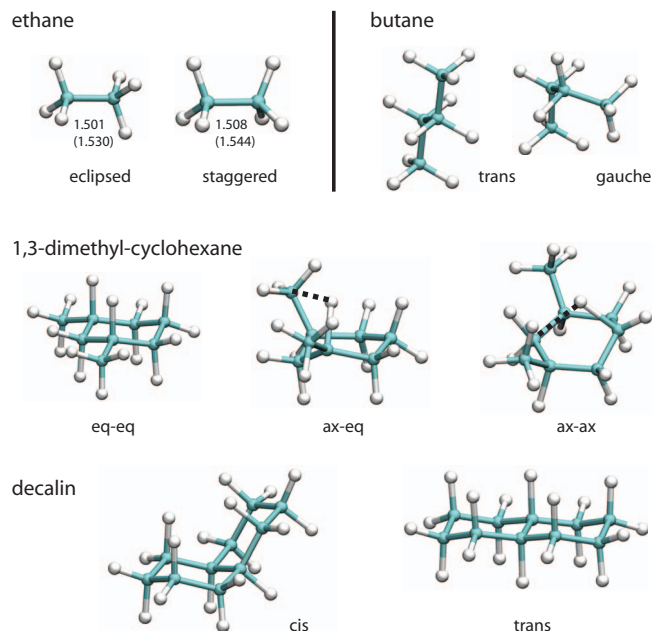
FIG. 9. eFF reproduces steric repulsions within a series of acyclic, cyclic, and fused cyclic alkanes. Overall the agreement with DFT relative energies is good, although there is slightly too much repulsion between carbon-carbon bonds.

the magnitude of these 1,3-diaxial interactions, we consider the relative energetics of axial-axial, axial-equatorial, and equatorial-equatorial 1,3-dimethylcyclohexane. The axial-equatorial and axial-axial geometries adopt an overly twisted geometry, a consequence of the too-large repulsion between axial methyl and axial hydrogen. Nonetheless the energy differences between these conformers closely match the DFT values (5.8 versus 5.9 kcal/mol DFT and 2.7 versus 2.1 kcal/mol DFT).

We also examine *cis* versus *trans* decalin. These two hydrocarbon conformers also differ in the number of interactions between axial substituents, but they are more rigid and less able to relax. In this case the energy difference is larger than the exact value (12.1 versus 3.2 kcal/mol DFT).

When a single bond is connected to a substituted double bond, a particularly strong steric interaction termed allylic 1,3-strain restricts the rotation about the single bond.[35] We consider two conformers of 2-pentene, noting that the minor form is substantially destabilized by the repulsion between methyl groups (Fig. 10). eFF estimates the energy difference
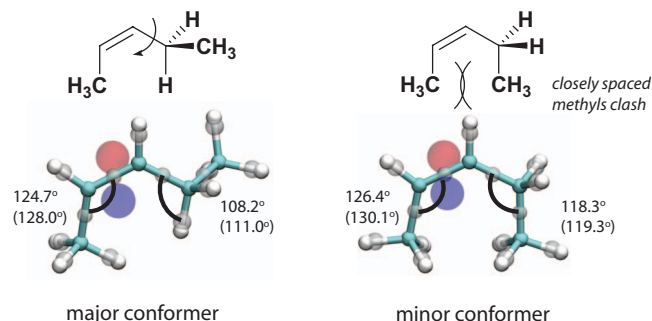

FIG. 10. A single bond attached to a substituted double bond finds its rotation severely restricted due to a steric interaction called allylic 1,3-strain. eFF reproduces the magnitude of this effect well.

between conformers to be slightly higher than the DFT value (5.5 versus 4.6 kcal/mol DFT). In this case, the too-high repulsion between methyl groups in eFF is balanced by the too-long double bond to give a value that agrees well with the known value.

Overall, eFF gives remarkably good estimates of the energy differences between hydrocarbon conformers. It is encouraging that the simple eFF functions can describe subtle conformational preferences of hydrocarbons as well as coarse properties such as bond formation and atom hybridization. This is noteworthy, considering the number of terms and parameters in a conventional force field[36] devoted solely to the task of computing preferred bond lengths, angles, and torsions within molecules.

E. Comparison of methyl cation, radical, and anion confirms difficulty handling *p*-like electrons

Although the discussion so far has focused on neutral closed-shell molecules, eFF can also describe cationic and anionic species and radicals. Since these species are the ones left over when bonds are broken, they need to be described accurately if we are to compute correct bond dissociation energies. As prototype molecules, we consider methyl cation, radical, and anion. We find that the geometric parameters of these species are reasonably close to exact values, but that the relative energetics of the methyl radical and anion is inaccurate due to the difficulty outlined in Sec. III C of representing *p*-like electrons.

As reference calculations, we cite high-level *ab initio* theory [CCSD(T)/aug-cc-pVTZ (Ref. 37)] in addition to DFT, since in DFT self-interaction effects may make it difficult to compute accurately the relative energies of molecules with orbitals containing one versus two electrons.

In terms of geometry, methyl cation is found to be planar by eFF, in agreement with DFT and CCSD(T), and the CH bond length matches the value from higher level theory as well [1.10 Å versus 1.09 Å DFT and 1.09 Å CCSD(T)]. Methyl radical is also found to be planar by eFF, DFT, and CCSD(T), and the CH bond length computed by the three methods is in good agreement as well [1.09 Å eFF versus 1.08 Å DFT and 1.08 Å CCSD(T)].

However, in methyl radical, eFF has difficulty describing the *p*-like unpaired electron, and as with the π electrons in ethylene, eFF makes the unpaired electron very diffuse ($s=4.44$ bohr) and places it above the molecular plane. This causes the adiabatic ionization potential to be substantially too low [64 kcal/mol eFF versus 227.4 kcal/mol DFT versus 226.8 CCSD(T)/aug-cc-pVTZ].

Methyl carbanion in eFF is unstable with a negative ionization potential for one of the lone pair electrons (−93 kcal/mol). Experimentally, in contrast, methyl carbanion is more stable than methyl radical, but only by 1.8 kcal/mol.[38] However, a very accurate description of electron correlation is required to capture this stability—CCSD(T) computes the energy difference properly (1.6 kcal/mol) but B3LYP fails to do so (−15.6 kcal/mol)—so it is not surprising that eFF fails to make methyl carbanion properly stable.

The overall instability of carbon radical and anion spe-

cies in eFF leads to an overestimation of carbon-carbon bond dissociation energy strengths, as we discuss further in Sec. III F.

F. Bond dissociation energy accuracy depends on nature of fragments

In eFF, the energy required to cleave a carbon-carbon bond into two radicals is too high, e.g., $D(H_3C-CH_3)$ = 163.5 kcal/mol versus 93.4 kcal/mol DFT and $D((CH_3)_3C-CH_3)$ = 121.4 kcal/mol versus 86.0 kcal/mol DFT. This results primarily from the poor description of CH_3 radical. In contrast, the eFF bond dissociation energy of H_2 is too low, 67.2 kcal/mol versus 110.0 kcal/mol DFT. We elaborate on these two cases further below.

Errors in homolytic bond dissociation energies arise from differences in how well the eFF wave functions represent the true electron density in the molecule versus separated fragments. For hydrogen molecule, the true electron density is a doubly peaked nucleus-centered function, which eFF describes as a singly peaked bond-centered function. Hydrogen atom in contrast is represented well, because in both eFF and in the true case, the electron density has a maximum at the nucleus.

In the ethane carbon-carbon bond, the errors in basis representation are reversed. Carbon-carbon sigma bonds have an electron density that is concentrated in the region between the nuclei; hence the eFF bond-centered representation is a good one. On the other hand, methyl radical is poorly represented because, as discussed in Sec. III E, eFF does not have the proper p functions to describe the radical electron. Hence the relative error is in the opposite direction compared with the H_2 case, and ethane is overbound.

For carbon-hydrogen bonds, the basis representation errors of the molecule versus the dissociated fragments cancel, and the bond dissociation energy is near the correct value $[D(H_3C-H)$ = 119.9 kcal/mol versus 111.6 kcal/mol DFT]. This good agreement persists even when additional substituents are present, e.g., $D((CH_3)_3C-H)$ = 108.2 kcal/mol versus 100.0 kcal/mol DFT.

Heterolytic bond dissociation can be described as well, where electron pairs split asymmetrically, so that one species is left with two electrons while the other is left with none at all. For the simplest protonation, the species HeH^+ has a bond dissociation energy near the exact value (44.1 kcal/mol versus 45.4 kcal/mol DFT). This excellent agreement comes about because the electron pair of HeH^+ is mainly centered on the helium, making the singly peaked eFF density a good approximation to the true electron density.

G. Reactions involving hydrogen; allowed versus forbidden reactions can be distinguished

Figure 11 shows two simple reactions involving rearrangements of hydrogen molecules and/or atoms; one is allowed, while the other is forbidden, where "forbidden" means that the energy of the transition state is greater than the energy needed to break all the bonds of the reactants. The
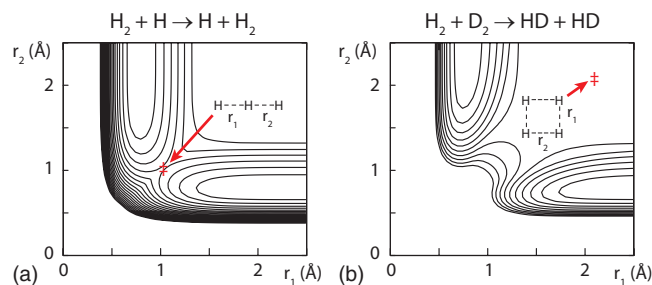

FIG. 11. eFF properly distinguishes between (a) the allowed $H+H_2 \rightarrow H_2+H$ reaction and (b) the forbidden $H_2+D_2 \rightarrow 2HD$ reaction. In the first case there is a low energy linear transition state with partial bonds to both hydrogens, while in the second case, both reactant bonds must be simultaneously broken in forming the transition state, making it prohibitively high in energy. Contour lines are separated by 10 kcal/mol in (a) and 20 kcal/mol in (b).

energy barrier of the "allowed reaction" is overestimated, but overall, eFF is able to determine the correct classification for the two reactions.

The allowed reaction is $H+H_2 \rightarrow H_2+H$. We find correctly that the transition state is collinear with a symmetric saddle point [at r=1.04 Å eFF versus 0.93 Å DFT, 0.93 Å HF/6-311g**, and 0.95 Å quantum Monte Carlo (exact)[39]]. The predicted energy barrier is 42 kcal/mol eFF versus 4.3 kcal/mol DFT, 17.5 kcal/mol HF/6-311g**, and 9.7 kcal/mol quantum Monte Carlo.

The forbidden reaction is $H_2+D_2 \rightarrow 2HD$. All of the paths that can lead from reactant to product are highly unstable,[25,40] as suggested by the Woodward–Hoffmann rules[41] for thermal $[2+2]$ concerted processes—for the sake of comparison, we constrain the reaction geometry to be rectangular. We find a square transition state with a relative energy of 132 kcal/mol, which can be compared with 209 kcal/mol DFT, 191 kcal/mol HF/6-311g**, and 147 kcal/mol multireference configuration interaction (MRD-CI, exact).[42] The transition state bond length is 2.21 Å for eFF versus 1.13 Å DFT, 1.11 Å HF/6-311g**, and 1.22 Å for MRD-CI.

Not all four-center metathesis reactions are forbidden; if an electropositive element is involved, the transition state becomes ionic in nature, and the reaction is allowed. For example, the reaction $LiH+D_2 \rightarrow LiD+HD$ has a low energy barrier (6.9 kcal/mol DFT), and is the basis for a process to create isotopically labeled lithium hydride.[43]

eFF correctly reproduces the trapezoidal geometry of the transition state, as well as the linear geometry of the precomplex intermediate (Fig. 12). As befits the ionic nature of the transition state, the eFF bonding electrons are localized along
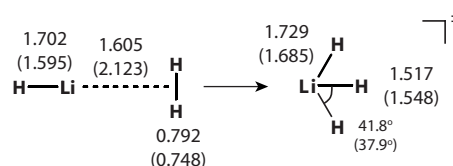

FIG. 12. Lithium hydride exchange reaction proceeds via formation of a precomplex intermediate, then exchange of atoms via a low barrier transition state with ionic character. eFF correctly reproduces the trapezoidal geometry of the transition state, but somewhat overestimates the barrier height for the reaction.
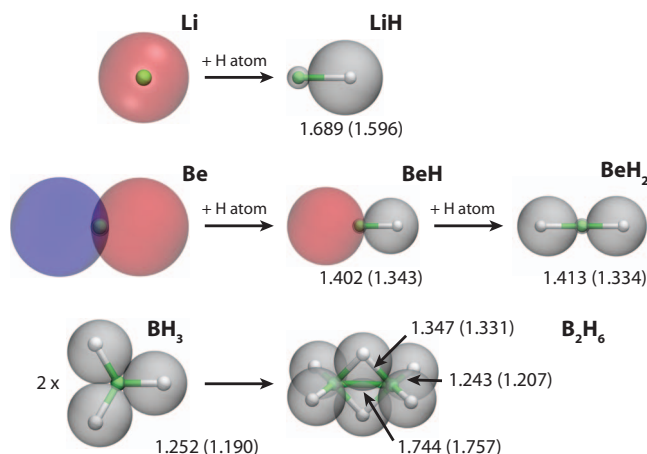
FIG. 13. Lithium, beryllium, and boron hydrides containing ionic and/or electron-deficient multicenter bonds. Bond lengths are in angstrom with DFT values in parentheses for comparison. eFF obtains correct geometries and dissociation energies for these systems—not surprising, as the electrons are s-like and well represented by eFF.

the Li–H bonds above and below the central hydrogen. eFF recognizes that the reaction is allowed, finding a reaction barrier of 13.4 kcal/mol relative to separated species, which is—as in the case with H_2+H—somewhat higher than the value from DFT (6.9 kcal/mol).

H. Ionic and multicenter bonds are well described

The elements lithium, beryllium, and boron often participate in ionic bonds, since they are electropositive; and also participate in electron deficient multicenter bonds, since they lack enough electrons to complete a full octet. Examples include lithium hydride, beryllium dihydride, and diborane (Fig. 13), which eFF generally describes well, as the bonding electrons are shifted only slightly away from the nuclei, and are thus to a good first approximation spherical and s-like.

Lithium atom with eFF adopts a $1s^2 2s^1$ configuration with a valence electron much larger ($s=7.45$ bohr) than the spin-paired core electrons ($s=0.71$ bohr). Lithium hydride has a bond length that is slightly too long (1.69 Å eFF versus 1.59 Å DFT) and a dipole moment that is slightly too high (6.51 D versus 5.70 D). The dissociation energy is very near the exact value (58.1 kcal/mol versus 58.2 kcal/mol DFT)

Beryllium dihydride is linear with a bond length of 1.41 Å eFF versus 1.33 Å DFT. The energy needed to break BeH_2 into BeH and H is near the DFT value (113.0 kcal/mol versus 97.5 kcal/mol DFT); however, the energy of breaking BeH into Be and H atoms is too high (109.6 kcal/mol versus 57.7 kcal/mol DFT). This too-high energy is a consequence of a well-known difficulty in describing the valence electrons of beryllium atom as a single configuration wave function[44] (in eFF, the $2s^2$ electrons in Be shift apart from each other as in a GVB wave function, but without any accompanying resonance stabilization).

The boron compound BH_3 dimerizes into the borane B_2H_6, which is stabilized by two three-center two-electron bonds. eFF describes nearly all aspects of the BH_3 and B_2H_6
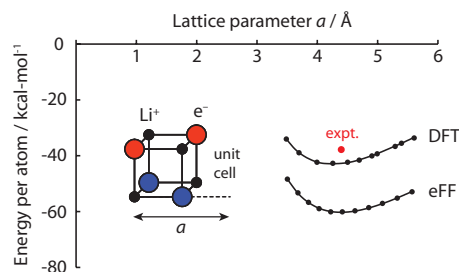

FIG. 14. Bonding in lithium bulk solid, showing single spin electrons nestled in octahedral interstices between fcc ions; the EOS is also shown and compared with DFT (Ref. 46).

geometries correctly (see Fig. 13). However, the dimerization energy is too low (27.6 kcal/mol versus 39.0 kcal/mol exact[45]).

I. Metals described accurately using interstitial electrons; the limiting case of a uniform electron gas

In eFF, metallic electrons are represented by diffuse electrons that nestle into the interstices between the ions. Interstitial sites in lithium metal are occupied by single electrons with random up- or down-spins (Fig. 14), while analogous sites in beryllium are occupied by electron pairs (Fig. 15). In the case of beryllium, the electron density distribution predicted by eFF agrees with those observed by x-ray crystallography[47] and calculated in two separate periodic DFT studies.[48,49]

eFF geometries and elastic constants of Li and Be metal agree well with experimental values (Table IV), but cohesive energies are too high, since the $2s$ electrons of isolated Li and Be atoms are poorly represented in eFF. There is precedent to describing metallic bonding using localized electrons, as in the *interstitial electron model* developed by McAdon and Goddard[50] and by Li and Goddard.[51] In these models, the valence electrons occupy interstices between crystal lattice sites, and interact as classical particles via effective potentials. Phonon dispersion relations in a variety of face-
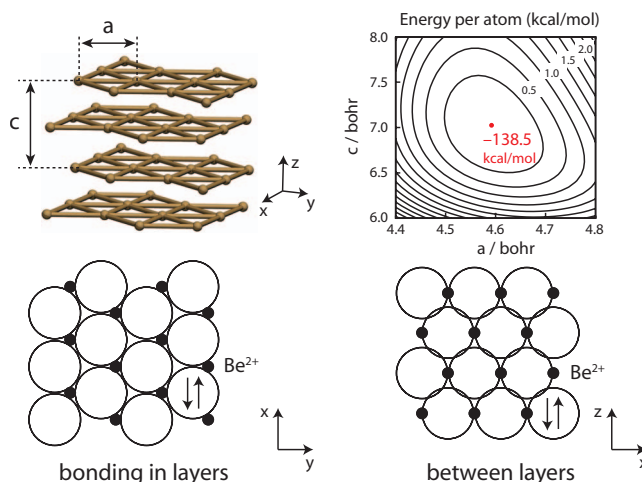

FIG. 15. Bonding in beryllium bulk solid, showing electron pairs forming strong bonds within and between layers in a hexagonal close packed array of ions; the EOS is also shown as a function of lattice parameters a and c.

TABLE IV. Lithium and beryllium parameters with a comparison of eFF and experimental values. Lattice constants are somewhat too large—we explain this after considering the energetics of a uniform electron gas—and cohesive energies are too high, because the bulk solid is represented more properly than the free atoms making up the metal. Elastic constants are nearly perfect.

		eFF	Expt.
Lithium	Lattice constant (Å)	4.42	4.40
	Bulk modulus (GPa)	12.2	13.0
	Cohesive energy (kcal/mol)	60	38
Beryllium	Lattice constant a (Å)	2.43	2.29
	Lattice constant c (Å)	3.72	3.59
	Bulk modulus (GPa)	121.9	110–127
	Poisson ratio	0.092	0.032
	Cohesive energy (kcal/mol)	138	77

centered cubic (fcc) metals were predicted and shown to agree well with experiment.

In the eFF description of bulk lithium, the Li^+ ions assume fcc lattice positions, and individual valence electrons occupy octahedral interstitial positions in between the ions. To optimize the overall spin configuration, we used a spin-swapping simulated annealing procedure (from 10 000 to 0 K over 10^4 steps), resulting in a net decrease in energy of only 2 kcal/mol/atom from an initial layered spin-polarized arrangement. The energy of the solid is only slightly dependent on the spin configuration of the system because of the relatively low overlap ($S = \int \psi_i \psi_j = 0.18$) between the interstitial electrons.

In bulk beryllium, the nuclei form a hexagonal close-packed structure, both in eFF and experiment. We observe strong bonding between atoms in the XY plane, the result of closed-shell electron pairs that occupy alternating threefold sites between Be^{2+} ions; this is reflected in the >100 GPa bulk modulus of the metal. The bonding between layers is strong as well, the result of vertical columns of alternating electrons and nuclei in the Z direction. The strong interlayer bonding results in an c/a ratio that is unusually small for hexagonal close-packed metals (1.53 versus the ideal value 1.66). eFF finds a ratio of 1.57, close to the experimental value [and DFT finds a c/a of 1.59 (Ref. 48)].

eFF can also be judged by its ability to reproduce the energetics of a uniform electron gas, the limiting case of electrons in a uniform neutralizing background charge. This system is defined by a single parameter, the Wigner–Seitz radius r_s, related to the electron density ρ by $\rho = (\frac{4}{3}\pi r_s^3)^{-1}$.

eFF describes the uniform electron gas as a close-packed lattice of localized electrons analogous to a Wigner[52] crystal packing, only stable at much higher electron densities. We considered several lattices, all of which led to similar energies [in hartrees per electron, open-shell NaCl (−0.047), open-shell sphalerite (−0.043), and closed-shell fcc (−0.041)], suggesting that the uniform electron gas in eFF has a fluxional character.

Figure 16 shows the energetics of the eFF NaCl-packed uniform electron gas compared with HF energies and exact energies taken from accurate quantum Monte Carlo calculations.[53,54] We find that eFF differs from the exact
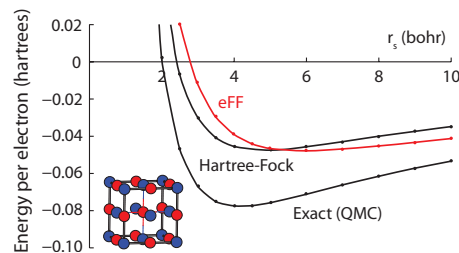

FIG. 16. Potential energy of a uniform electron gas with respect to the density parameter r_s. eFF agrees with the binding energy from HF, but neglects the correlation energy which would cause it to agree with the exact curve.

curve, but matches the well depth of the HF to within 0.005 hartree/electron, consistent with the mean-field nature of, and consequent neglect of electron correlation in, both HF and eFF. Additionally, the eFF curve is stretched out so that the minimum energy occurs at $r_s \sim 6.1$ bohr compared with 4.8 bohr for HF. This may explain the slightly expanded lattice constants observed in eFF-optimized bulk lithium and beryllium.

IV. RESULTS FOR ELECTRONICALLY EXCITED SYSTEMS

A. Thermodynamics of warm dense hydrogen

We summarize here the results reported previously in Ref. 16 and also add new comparisons to recent experimental data.[55] The behavior of hydrogen at extreme pressures (hundreds of gigapascals) and moderate temperatures (thousands of degrees) has relevance to the phase partitioning of giant planetary interiors,[56] as well as the design of systems for inertial confinement fusion.[57] Warm dense hydrogen has been discovered to have metallic properties (3000 K, 140 GPa),[58] and it has been proposed that its enhanced conductivity may involve the participation of electronically excited mixtures of H_2 molecules, H atoms, and other species along with free protons and electrons.[58] It has also been proposed that at somewhat higher temperatures and lower densities ($T = 15\,300$ K and $r_s = 2$ bohr), a *plasma phase transition* occurs, where dissociation of molecules and ionization of atoms occur simultaneously.[59] However, the properties of warm dense hydrogen remain poorly understood, due to the challenges of producing and characterizing hydrogen under such conditions, and the difficulty in modeling systems that may contain complex mixtures of molecules, atoms, ions, and excited electrons.

We have used eFF to study the thermodynamics of dense hydrogen over pressure and temperature ranges that include the warm dense state of interest. Pressures and temperatures are extracted from dynamics simulations using classical virial expressions, e.g., $\frac{3}{2}k_B T = 1/N_{\text{nuc}} \langle \sum_i \frac{1}{2} m_i v_i^2 \rangle$ and $PV = N_{\text{nuc}} k_B T + \frac{1}{3}\langle \sum_i x_i \cdot \partial E/\partial x_i \rangle$, where we sum over all nuclear and electronic degrees of freedom and take $m_{\text{elec}} = m_{\text{nuc}}$ [since we are primarily interested in equilibrium thermodynamics; m_{elec} was decreased with no effect on the equation of state (EOS)].

As validation, we have compared eFF EOSs with those obtained from static and dynamic compression experiments.
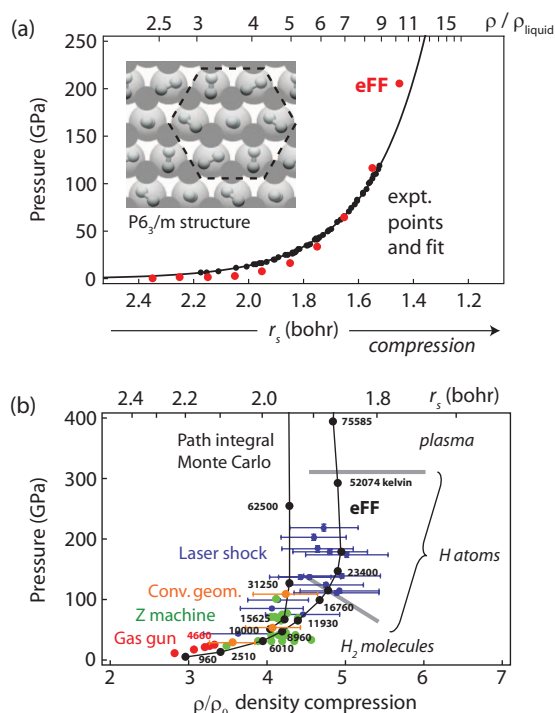
FIG. 17. Comparison of eFF EOS to the ones from experiments where hydrogen is compressed (a) statically or (b) dynamically. In (a), the eFF EOS of solid hydrogen at 300 K matches the data from diamond anvil experiments (Ref. 60). In (b) the eFF single shock Hugoniot curve for liquid H_2 (solid black line) agrees with the data from many experiments: gas gun (Ref. 62) (red dots), Z machine (Ref. 63) (green dots), convergence geometry (Ref. 64) (orange), and laser ablation (Ref. 55) (blue). Note that the eFF results were published in 2007, while the results from laser ablation experiments (which agree well with eFF but not path integral theory) were published in 2009.

In static experiments, hydrogen is compressed in a diamond anvil cell to extremely high densities (greater than ten times liquid density,[60,61] at 300 K, and over the density range r_s = 1.4–2.2 bohr (i.e., solid hydrogen), we found excellent agreement between the EOS from eFF and that from experiment [Fig. 17(a)].

In dynamic experiments, hydrogen is compressed using shock waves produced by chemical explosives, magnetic pinching, or laser ablation; the maximum compression is less than in static experiments (four to five times liquid density in a single shock), but higher temperatures can be reached [30 000–50 000 K (Ref. 55)], making it possible to probe the hydrogen dissociation/ionization regime. A shock wave passing through a material with internal energy E_0, density ρ_0, and pressure p_0 causes a jump in these parameters ahead of the shock front. If a thermodynamic equilibrium is established in the bulk material on both sides of the shock front, the new E, ρ, and p satisfy the Rankine–Hugoniot relations

$$E - E_0 + \frac{1}{2}\left(\frac{1}{\rho} - \frac{1}{\rho_0}\right)(p + p_0) = 0. \tag{26}$$

We computed a single shock Hugoniot curve using eFF and found excellent agreement with all available experimental results [Fig. 17(b)].

Hugoniot curves, plotted as density versus pressure, take on a characteristic form: they curve gently upward, then in-

flect up sharply at a maximum compressibility determined by the nature of bonding in the material. As a reference point, an ideal gas of diatomic molecules has $\rho_{max}/\rho_0 = 6$, while an ideal gas of atoms has $\rho_{max}/\rho_0 = 4$. At the time we published our communication (2007), diverse experiments (shocks from gas gun,[62] Z-machine,[63] and convergent explosives[64]) supported a Hugoniot that inflected upward by 50 GPa to a compressibility of $\rho/\rho_0 \sim 4 \pm 0.6$. The experimental data were limited to pressures less than 100 GPa; however, path integral Monte Carlo [PIMC (Refs. 65–67)] calculations suggested that the compressibility remained near 4 up to a pressure of at least 500 GPa.

Our calculations, however, predicted a maximum compressibility of 4.94 at 179 GPa; although this appeared to be a discrepancy, the lack of experimental data at higher pressures (>100 GPa) made it difficult to say whether or not eFF was correct. Very recently (2009), measurements at higher pressures—220 GPa—have been made using laser ablation as a shock source,[55] which indicate a compressibility of ~4.2 below 110 GPa, rising to a maximum compression of 5 at 160 GPa, in excellent agreement with our prior prediction. Indeed, the eFF single shock Hugoniot curves smoothly in such a way that it passes through the error margins of nearly all of the available experimental data.

To understand the origin of the higher maximum compressibility predicted by eFF, we analyzed the composition of hydrogen at different points along the Hugoniot curve, studying the proportions of molecules, atoms, and plasma present. We find, in particular, that the region over which hydrogen atoms interact strongly with each other extends to quite high temperatures and pressures, the result being that at 400 GPa and 75 000 K, the compressibility remains high ($\rho/\rho_0 = 4.84$), intermediate between an ideal monoatomic and an ideal diatomic fluid. The heightened stability of a molecularlike phase may result from the transient formation of a metallic phase, where electrons hop freely between hydrogen atoms and molecules; we can observe with eFF this electron hopping behavior. Overall, the phenomenon of electron hopping provides an explanation for the enhanced reflectivity of dense hydrogen observed above 25 GPa in several experiments,[55,68] and may contribute to the enhanced compressibility of dense hydrogen (relative to an ideal gas of atoms) along the primary shock Hugoniot.

It remains to explain the discrepancy between the Hugoniot obtained with eFF versus other theoretical methods such as PIMC. In order to determine the regimes over which eFF might be expected to be most accurate, we computed isothermal EOS at different densities with eFF, and compared them with EOS from two theories: (1) the Saumon–Chabrier model,[59] a linear-mixing model that interpolates between molecular, atomic, and plasma EOSs—we expect it to be most accurate in its extremes, i.e., the limits of purely molecular or weakly coupled plasma phases, and (2) PIMC,[65–67] which is expected to be more accurate at high temperatures due to the improved convergence of the thermal density matrix and simplified nodal structure for the trial wave function. We find that for the molecular and atomic phases, eFF agrees quite well with the chemical model and with the PIMC model in their respective regimes of validity
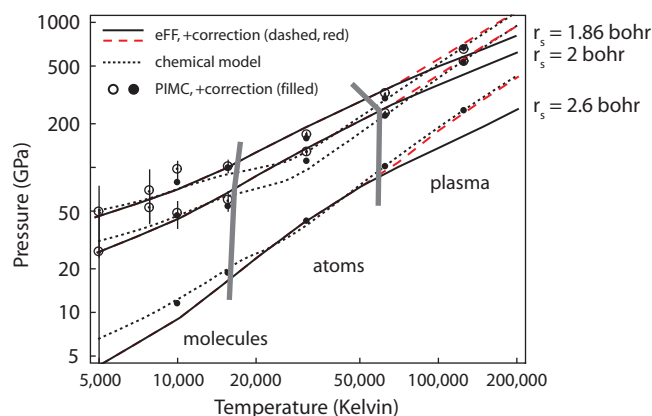
FIG. 18. Comparison of EOS from eFF to other theoretical methods for fixed densities ($r_s = 1.86, 2, 2.6$ bohr, corresponding to $\rho/\rho_{liquid} = 4.9, 3.9, 1.8$) and varying temperatures, showing good agreement in the regimes where the other theories are expected to be the most accurate. Specifically, eFF (solid line) matches the EOS from the Saumon–Chabrier chemical model [dotted line (Ref. 59)] in the molecular regime, and the EOS from PIMC calculations [circles, where solid indicates the EOS with energy and pressure corrections to obtain the correct dissociation energy for hydrogen molecules (Refs. 65–67)] in the atomic regime.

(Fig. 18); for the plasma phase, the agreement is good if we use an ideal gas correction to account for the pressure from fully ionized electrons.

There are two limits where the eFF EOS is less accurate due to the limitations of the Gaussian wave packet representation: low densities ($r_s > 2.6$ bohr) at low temperatures (molecular) and high temperatures (weakly coupled plasma limit); both these limits lie well outside the domain of the Hugoniot curve plotted in Fig. 17(b). Particularly accurate from eFF is the transition between molecular and atomic phases, which is difficult to capture with PIMC due to its inaccuracy at lower temperatures, and also difficult to capture with the chemical model, due to the uncertainty of mixing parameters in that regime.

In conclusion, the simple eFF, with no special parametrization for hydrogen, provides a unified and continuous description of solid molecular, liquid molecular, atomic, and ionized phases of hydrogen over temperatures from 300 to 200 000 K, and densities from 0.34 to 1.7 g/cm³ (two to ten times liquid density). The eFF EOS appears to be particularly accurate in the intermediate regime corresponding to the controversial region of the Hugoniot (100–300 GPa and

15 000–50 000 K), which we predict represents a complex mixture of phases: the end of a transition from a molecular to an atomic fluid, the start of a transition from an atomic fluid to a plasma, and metallic character in that bound electrons can hop freely between atoms via transient formation of polyatomic species.

B. Auger relaxation in core-ionized diamondoids

We summarize here the results reported previously in Ref. 17. In the Auger process, a core electron is removed from an atom, which in turn causes a valence electron to collapse inward into the core, and another valence electron (the Auger electron) to be ejected.[69] We examine two phenomena associated with the Auger process. First, when the Auger process is triggered in a material by high energy photons or electrons, Auger electrons are released from surface layers, but not from the bulk of the solid [Fig. 19(b)]—thus, Auger spectroscopy, where the energy distribution of the emitted electrons is examined, is a useful surface characterization method. Second, selective bond breaking[71] may occur at the site of the core hole as it relaxes [Fig. 19(a)]; understanding this process better would be useful for developing semiconductor fabrication methods where electrons rather than heavy ions are used to etch fine features into materials.[72,73]

eFF describes both bond breaking and electron emission in the Auger process. As a model system, we considered a diamond nanoparticle $C_{197}H_{112}$, which is fully saturated on the surface with hydrogen atoms and roughly spherical. This nanoparticle contains six distinct layers, ranging in depth from the center of the particle to the surface.[74] By ionizing core electrons from atoms in each of these layers, we study surface versus bulk effects, in particular, how readily Auger electrons can be trapped inside a bulk material, and over what ranges surface bonds can be broken as a result of a core ionization.

In $C_{197}H_{112}$, we ionized core electrons from carbon atoms at different depths in the particle, which contained six different layers of carbons; 5940 dynamics trajectories were simulated. We found clear evidence of Auger-induced bond breaking: ionizing a surface carbon atom would cause attached hydrogens to be ejected over less than 10 fs, and
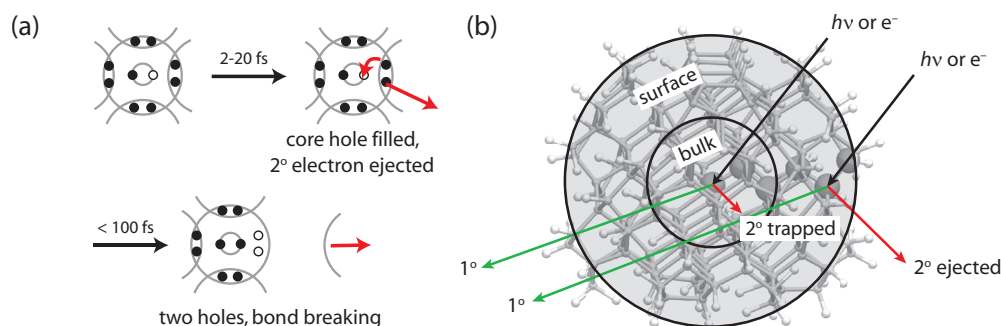

FIG. 19. Phenomena associated with Auger processes modeled using eFF: (a) bond breaking and desorption of surface fragments as a result of core-hole relaxation, which may occur via an intermediate state containing two valence holes [Knotek–Feibelman mechanism (Ref. 70)]; and (b) the surface selectivity of Auger spectroscopy, which exists because secondary Auger electrons arising from surface layers are ejected and subsequently detected, while those from bulk atoms are trapped in the solid.
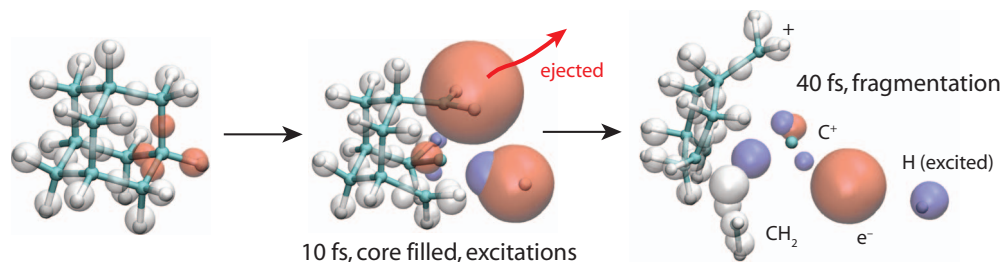
FIG. 20. eFF predicted Auger fragmentation of core-ionized adamantane, showing a single trajectory in which the molecule was equilibrated at 300 K for 500 fs (time step of 5 as), a $1s$ core electron was instantaneously removed, and the dynamics was propagated for 100 fs (time step of 1 as).

sometimes the heavy atom itself would detach as well. This led to the production of H^+ ions and H atoms, as well as CH and CH_2 molecular fragments.

   Ionizing subsurface atoms caused surface bonds to break as well via a remote heating effect. In these cases, we observed H^- ions exclusively and found that they separated at arbitrary times over the 100 fs duration of the simulations. This effect was hinted at in an experiment involving the photon-stimulated desorption of H^+ and H^- ions from hydrogen-terminated diamond surfaces.[75] The experimental results suggested that H^- ions were released via an indirect mechanism involving secondary electrons as an intermediary versus H^+ ions which were produced via a direct mechanism related to the core excitation, both consistent with the eFF simulation results.

   In addition to bond breaking, we also observed electron emission in the Auger process—once electrons are ejected, their size grows linearly with time, as expected from a free electron wave packet. Plotting the distribution of free electron energies, we found an Auger peak of fast electrons produced when carbons in the outer three layers (~ 3 Å) were ionized. Ionizations deeper down created excited valence electrons, but they were trapped and equilibrated by the surrounding bulk over tens of femtoseconds. This is consistent with the known surface selectivity of Auger spectroscopy.[74]

   To study the detailed mechanism of Auger-induced bond breaking, we examined the coupled electron and nuclear motions of core-ionized adamantane ($C_{10}H_{16}$), as shown in Figs. 20 and 21. At time zero, a $1s$ core electron is instantaneously removed from a carbon atom, which causes the four sur-

rounding valence electrons with the same spin as the ionized electron to collapse inward. These four electrons fall in toward the core hole together until one electron fills the hole, causing the other three to bounce away from the core as a result of Pauli repulsion. This leads to the escape of one electron and the excitation of the other two electrons, and at ~ 20 fs, the fragmentation of the bonds surrounding the original core ionization. An adjustable parameter—the dynamic electron mass—fixes the overall time scale of these events, but the nature and sequence of the events themselves are independent of this parameter.

   From 410 core-ionized adamantane trajectories, we found three mechanisms for bond breaking via electron excitation (Fig. 22). In 61% of the cases, a *direct Auger process* occurred where the hydrogen bound to the excited carbon was ejected either as a highly excited atom or as an H^+ ion. This resulted from a transient disruption of the electron density which persisted long enough for the bond to break, followed by limited recombination with the departing fragments to produce both neutral and ionic species.

   In another 32% of the trajectories, an *indirect thermal process* occurred where general electron excitations caused hydrides to slowly leak off the surface during the entire 100 fs trajectory. Finally, in 7% of the cases, a *secondary impact process* occurred where an ejected or excited Auger electron scattered off CH bonding electrons, leading to ionization of the electrons and release of H^+.

   Hence with eFF we reproduce the microscopic dynamics of Auger fragmentation: core hole filling, secondary electron ejection, and bond breaking in excellent agreement with available data. This procedure makes it possible to study the details of chemistry and electron energy redistribution processes that were previously impractical to simulate on a large scale.

V. CONCLUSION

   We have presented a simple method for describing excited electronic systems in terms of the dynamics of Gaussian wave packets. The key improvement over existing fermionic MD methods is our parametrization of a spin-dependent Pauli potential that is both simple and fast to compute, and accurate enough to describe a variety of materials containing covalent, ionic, multicenter. and/or metallic bonds. eFF occupies a niche between conventional electronic structure and classical plasma methods: it can simulate moderate excitations (tens to hundreds of electron volts) that vary sharply
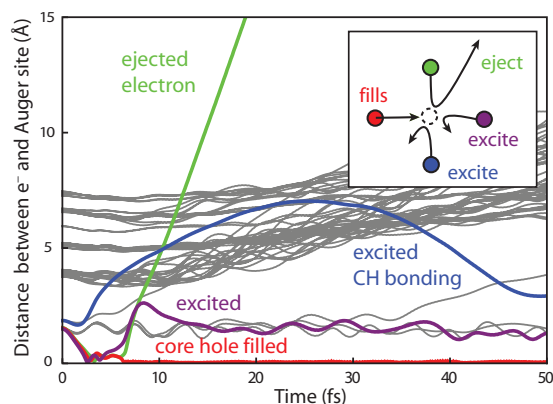

FIG. 21. Electron dynamics during the Auger process. The red valence electron fills the core hole after 7 fs, the green electron is ejected after 12 fs, and the blue and purple electrons remain excited but bound over 50 fs.
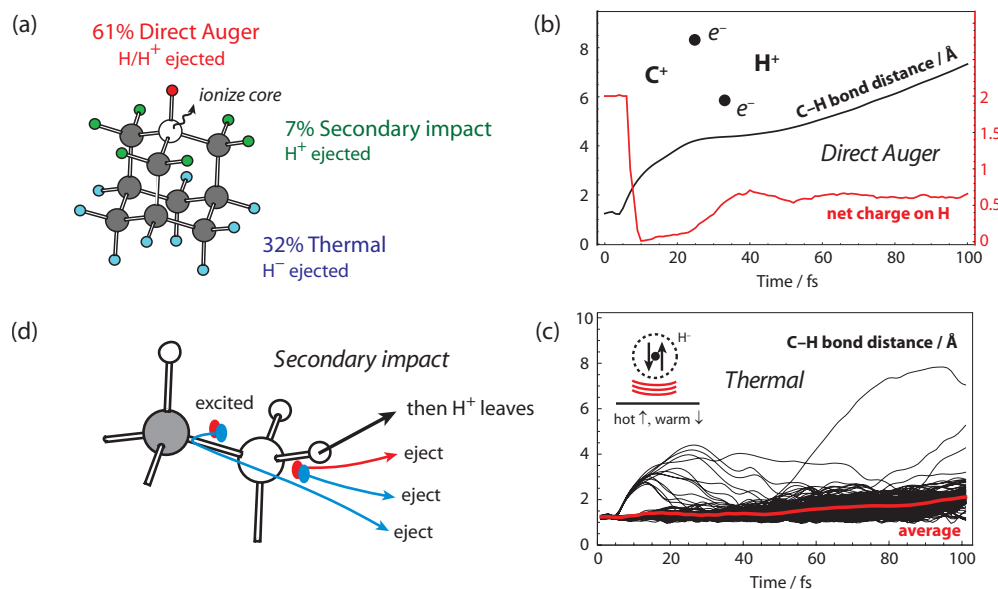
FIG. 22. Mechanisms of hydrogen desorption summarized. (a) The analysis was based on 410 trajectories of core-ionized adamantane ($C_{10}H_{16}$). We distinguish three mechanisms using the following decision tree: if the ejected hydrogen was bound to the core-ionized atom, classify the event as the result of a direct Auger process. If not, examine whether more than two electrons were ever associated with the ejected proton at any point in the trajectory. If yes, classify the event as the result of a secondary impact process, otherwise classify it as a thermal process. (b) Direct Auger processes involve a transient (10–20 fs) depletion of charge to form a two valence-hole state, followed by limited recombination to produce H^+ ions or H atoms. (c) Thermal processes involve a slow leakage of H^- ions from the molecule. (d) Secondary impact processes involve the scattering of an excited electron off an adjacent pair of bonding electrons, resulting in ionization of the bonding electrons and prompt ejection of an H^+ ion.

over space and time, in large systems (tens of thousands of atoms) where strong couplings between nuclei and electrons exist, and chemistry occurs. It is particularly well suited to study interfaces between highly excited and nonexcited materials, heterogeneous mixtures of phases, and nonequilibrium excitations driven by extremes of temperature, pressure, or radiation.

In one application of eFF, we characterized the transformation of dense hydrogen from a solid to a molecular liquid to an atomic liquid to a plasma over temperatures from 300 to 200 000 K, and densities from 0.34 to 1.7 g/cm^3 (two to ten times liquid density). We found that eFF is particularly accurate in describing the thermodynamics of the atomic liquid phase, probed by recent dynamic compression experiments; we find this phase is composed of a complex mixture of atoms, molecules, plasma, and electrons that hop from one nucleus to another, suggestive of a metallic character.

In another application, we examined the Auger decay process in a diamond nanoparticle. In this study, we created core holes (>200 eV) in the particle, which violently excited and ionized surrounding valence electrons, and heated the remaining electrons in the particle by tens of thousands of degrees. Core holes created at different depths from the surface induced dramatically different effects in the solid, both in terms of electron trapping versus emission—secondary electrons in the inner three layers were trapped, while those created in the outer three layers were ejected—and in terms of fragmentation of surface bonds—bulk excitations released hydride ions by indirect and nonspecific heating, while surface excitations ejected protons and hydrogen atoms by direct excitation, ionization, or scattering away of bonding electrons.

These results suggest that eFF can be used to probe the

properties of complex highly excited systems, with the expectation of qualitative accuracy sufficient to understand mechanisms, and in some cases even semiquantitative or quantitative accuracy. We expect that further improvements to eFF are necessary to describe a wider range of excitations more accurately, and to describe a wider range of materials more accurately.

For excitations, in the Auger study, eFF captured the microscopic steps and overall outcome of the Auger process well, but with a too-fast overall time scale. Increasing the dynamic mass of the electron helps to compensate, but a more general scheme may be needed to describe systems in which excitations are characterized by several time scales.

For materials, eFF assumes that kinetic energy differences dominate the overall exchange energy, which is true only when the electrons present are nearly spherical and nodeless. This assumption is valid for covalent compounds such as dense hydrogen, hydrocarbons, and diamond; alkali metals such as lithium and beryllium and semimetals such as boron; and various compounds containing ionic and/or multicenter bonds, such as boron dihydride.

However, electrons with substantial p character are poorly described, both because of limitations in the underlying wave packet representation, and also because kinetic energy differences no longer dominate exchange, so that the Pauli potential becomes inaccurate. Hence multiple bonds, radical electrons, and lone pairs are not properly represented—they are too diffuse, too easily ionized, and generally less stable than they should be (e.g., neon will spontaneously ionize).

One consequence of the instability of radicals, and of the limitations in basis functions, is that bond dissociation energies are inaccurate, and also relative transition state energies

for reactions where bonds are being broken and reformed. For example, in reactions between H_2 and H, allowed versus forbidden reactions can be distinguished, but the transition state energies are in error by tens of kcal/mol. At this point, eFF would have difficulty describing accurately most chemical reactions.

There are two tasks at which the current eFF excels. The first is computing the relative thermochemistry of isodemic reactions and conformational changes, where the bonds of the reactants are of the same type as the bonds of the products. For example, the section on conformational analysis illustrated that eFF could compute accurately both barrier hindering the internal rotation of ethane, as well as the relative energy difference between chair and boat conformations of cyclohexane. However, existing *ab initio* and density functional methods have solved this problem essentially exactly, so there is not much to be gained at applying eFF to this class of problems, except for validation purposes.

The second task is the one we have focused on in this paper—computing the properties of materials at extreme conditions, where electron excitations can change significantly the nature of bonding in the system. eFF can capture with surprising accuracy the behavior of such systems because it describes consistently and in an unbiased fashion many different kinds of bonds—covalent, ionic, multicenter, ionic, plasma—and how they interconvert and/or change when they become excited. Consider, for example, how eFF represents compressed lithium being heated from a solid to a liquid, and then a plasma: the electrons initially pack regularly between the ions, then become more irregularly distributed and expand as the metal liquefies, and finally move freely among the ions in the dense plasma. In contrast, in a conventional electronic structure calculation, an extensive set of high angular momentum and diffuse basis functions would be needed to capture the transition, possibly augmented with plane waves, and the computation would likely be biased toward one state or the other. The underlying concept behind eFF is that the basis representation and potentials may be overly simplistic, but they are consistent enough ("consistently bad") that a significant cancellation of errors takes place, and the overall result is quite accurate.

Future improvements to the accuracy and scope of eFF we expect will be made along two directions. First, we wish to develop better orbital-dependent exchange and correlation functions to describe lone pairs, multiple bonding, and higher Z atoms with chemical accuracy. These functions would be parametrized to reproduce the thermochemistry of a variety of materials in their ground state. Second, we wish to obtain a better understanding of multibody interactions in excited systems to discover how to appropriately set parameters like effective electron masses. We hope that the formulation presented here, as well as its successors, will enable the simulation of a wide range of interesting excited electron chemistry on realistic systems.

ACKNOWLEDGMENTS

APPENDIX: EWALD SUM FOR GAUSSIAN CHARGE DENSITIES

The goal is to compute the electrostatic interaction energy of a periodic set of Gaussian charge densities

$$\rho_i(\mathbf{r}) = q_i \sum_{\mathbf{R_L}} e^{-\alpha_i(\mathbf{r} - \mathbf{r_i} - \mathbf{R_L})^2}, \tag{A1}$$

where $\mathbf{R_L}$ is a set of periodic lattice vectors. The Ewald sum is

$$E = E_{\text{k-space}} + E_{\text{r-space}} + E_{\text{self}} + E_{\text{uniform}} + E_{\text{dipole}}. \tag{A2}$$

To compute $E_{\text{k-space}}$ and $E_{\text{r-space}}$, we break the density down into $\rho = \rho_1 + \rho_2$, where

$$\rho_1 = N e^{-\alpha r^2} - N_{\max} e^{-\alpha_{\max} r^2}, \tag{A3}$$

$$\rho_2 = N_{\max} e^{-\alpha_{\max} r^2}, \tag{A4}$$

and where $\alpha_{\max}$ is a threshold exponent; the default value for $\alpha_{\max}$ is $1/(3.54 \text{ bohr}^2)$. We sum ρ_1 over a real space lattice and sum ρ_2 over a reciprocal space lattice. Since ρ_1 is neutral for large r and localized to a small region of real space, the real space sum converges quickly in r. Since ρ_2 is diffuse for a small enough $\alpha_{\max}$, the reciprocal space sum converges quickly in k.

The reciprocal space energy $E_{\text{k-space}}$ is defined as

$$E_{\text{k-space}} = \frac{2\pi}{V} \sum_k \rho(\mathbf{k}) \rho_{\max}(\mathbf{k}), \tag{A5}$$

where

$$\rho(\mathbf{k}) = \sum_i q_i e^{-k^2/4\alpha_i} e^{-i\mathbf{k} \cdot \mathbf{r_i}}, \tag{A6}$$

$$\rho_{\max}(\mathbf{k}) = \begin{cases} \rho(\mathbf{k})|_{\alpha_i = \alpha_{\max}} & \text{for } \alpha_i > \alpha_{\max} \\ \rho(\mathbf{k}) & \text{otherwise} \end{cases}. \tag{A7}$$

The real space energy $E_{\text{r-space}}$ is defined as

$$E_{\text{r-space}} = \sum_{\mathbf{R_L}} \sum_{i \neq j} E_{ij}(\mathbf{r_{ij}} - \mathbf{R_L}), $$

where

$$E_{ij} = \frac{1}{r_{ij}} \text{erf} \sqrt{\frac{\alpha_i \alpha_j}{\alpha_i + \alpha_j}} r_{ij}, \tag{A8}$$

$$- \frac{1}{r_{ij}} \text{erf} \sqrt{\frac{\alpha_i \alpha_j^{\max}}{\alpha_i + \alpha_j^{\max}}} r_{ij}. \tag{A9}$$

In the real space sum, only interactions between a charge and another charge with $\alpha > \alpha_{\max}$ are considered.

The self energy E_{self} is the energy of a Gaussian charge with itself—this quantity must be subtracted out, since in reality, charges do not repel themselves. It is computed as follows:

$$E_{self} = -\frac{1}{2}\sum_i q_i^2 \frac{2}{\sqrt{\pi}}\begin{cases} \sqrt{\dfrac{\alpha_i \alpha_{max}}{\alpha_i + \alpha_{max}}} & \alpha_i < \alpha_{max} \\[2mm] \sqrt{\dfrac{\alpha_i \alpha_i}{\alpha_i + \alpha_i}} & \text{otherwise.} \end{cases} \quad (A10)$$

The uniform energy $E_{uniform}$ represents the interaction of each Gaussian charge with the uniform neutralizing background charge,

$$E_{uniform} = \frac{1}{4}Q\sum_i \frac{\pi}{V}\left(\frac{1}{\alpha_{max}} - \frac{1}{\alpha_i}\right) \quad \text{for } \alpha_i > \alpha_{max}. \quad (A11)$$

Finally, the dipole energy E_{dipole} neutralizes the net dipole of the unit cell,

$$E_{dipole} = \frac{2\pi}{3V}\left|\sum_i q_i\mathbf{x_i}\right|^2. \quad (A12)$$

[1] N. L. Doltsinis, *Quantum Simulations of Complex Many-Body Systems: From Theory to Algorithms*, Lecture Notes, edited by J. Grotendorst, D. Marx, and A. Muramatsu (John von Neumann Institut für Computing, Julich, Germany, 2002), Vol. 10, p. 377.

[2] J. C. Tully, J. Chem. Phys. **93**, 1061 (1990).

[3] A. Castro, M. A. L. Marques, J. A. Alonso, G. F. Bertsch, and A. Rubio, Eur. Phys. J. D **28**, 211 (2004).

[4] M. Lindenblatt and E. Pehlke, Phys. Rev. Lett. **97**, 216101 (2006).

[5] E. Livshits and R. Baer, J. Phys. Chem. A **110**, 8443 (2006).

[6] J. M. Dawson, Rev. Mod. Phys. **55**, 403 (1983).

[7] E. J. Heller, J. Chem. Phys. **62**, 1544 (1975).

[8] K. Singer and W. Smith, Mol. Phys. **57**, 761 (1986).

[9] M. Ben-Nun, J. Quenneville, and T. J. Martinez, J. Phys. Chem. A **104**, 5161 (2000).

[10] H. Feldmeier and J. Schnack, Rev. Mod. Phys. **72**, 655 (2000).

[11] D. Klakow, C. Toepffer, and P.-G. Reinhard, J. Chem. Phys. **101**, 10766 (1994).

[12] W. Ebeling and B. Militzer, Phys. Lett. A **226**, 298 (1997).

[13] M. Knaup, P.-G. Reinhard, C. Toepffer, and G. Zwicknagel, J. Phys. A **36**, 6165 (2003).

[14] M. Knaup, P.-G. Reinhard, and C. Toepffer, Contrib. Plasma Phys. **41**, 159 (2001).

[15] B. Jakob, P.-G. Reinhard, C. Toepffer, and G. Zwicknagel, Phys. Rev. E **76**, 036406 (2007).

[16] J. T. Su and W. A. Goddard III, Phys. Rev. Lett. **99**, 185003 (2007).

[17] J. T. Su and W. A. Goddard III, Proc. Natl. Acad. Sci. U.S.A. **106**, 1001 (2009).

[18] T. Maruyama, A. Ohnishi, and H. Horiuchi, Phys. Rev. C **45**, 2355 (1992).

[19] W. A. Beck and L. Wilets, Phys. Rev. A **55**, 2821 (1997).

[20] C. L. Kirschbaum and L. Wilets, Phys. Rev. A **21**, 834 (1980).

[21] J. S. Cohen, Phys. Rev. A **57**, 4964 (1998).

[22] A. A. Frost, J. Chem. Phys. **47**, 3707 (1967).

[23] See EPAPS supplementary material at http://dx.doi.org/10.1063/1.3272671 for the supporting information for origins of key energy expressions, energy curves, and geometries including electron positions of nonperiodic and periodic systems referred to in this paper.

[24] W. Kolos and L. Wolniewicz, J. Chem. Phys. **43**, 2429 (1965).

[25] C. W. Wilson and W. A. Goddard III, J. Chem. Phys. **56**, 5913 (1972).

[26] V. F. Weisskopf, Science **187**, 605 (1975).

[27] D. H. Boal and J. N. Glosli, Phys. Rev. C **38**, 1870 (1988).

[28] L. Wilets, E. M. Henley, M. Kraft, and A. D. Mackellar, Nucl. Phys. **A282**, 341 (1977).

[29] C. Dorso, S. Duarte, and J. Randrup, Phys. Lett. B **188**, 287 (1987).

[30] S. Izvekov, J. M. J. Swanson, and G. A. Voth, J. Phys. Chem. B **112**, 4711 (2008).

[31] JAGUAR, version 7.0, Schrodinger, LLC, New York, NY, 2007.

[32] J. Paier, M. Marsman, and G. Kresse, J. Chem. Phys. **127**, 024103 (2007).

[33] A. A. Frost and R. A. Rouse, J. Am. Chem. Soc. **90**, 1965 (1968).

[34] J. G. Hamilton and W. E. Palke, J. Am. Chem. Soc. **115**, 4159 (1993).

[35] R. W. Hoffmann, Chem. Rev. (Washington, D.C.) **89**, 1841 (1989).

[36] B. R. Brooks, R. E. Bruccoleri, B. D. Olafson, D. J. States, S. Swaminathan, and M. Karplus, J. Comput. Chem. **4**, 187 (1983).

[37] D. A. Dixon, D. Feller, and K. A. Peterson, J. Phys. Chem. A **101**, 9405 (1997).

[38] G. B. Ellison, P. C. Engelking, and W. C. Lineberger, J. Am. Chem. Soc. **100**, 2556 (1978).

[39] D. Diedrich and J. B. Anderson, J. Chem. Phys. **100**, 8089 (1994).

[40] C. W. Wilson, Jr. and W. A. Goddard III, J. Chem. Phys. **51**, 716 (1969).

[41] R. B. Woodward and R. Hoffmann, J. Am. Chem. Soc. **87**, 395 (1965).

[42] A. I. Boothroyd, P. G. Martin, W. J. Keogh, and M. J. Peterson, J. Chem. Phys. **116**, 666 (2002).

[43] K. E. Wilzbach and L. Kaplan, J. Am. Chem. Soc. **72**, 5795 (1950).

[44] A. G. H. Barbosa and M. A. C. Nascimento, Int. J. Quantum Chem. **99**, 317 (2004).

[45] J. D. Dill, P. von R. Schleyer, and J. A. Pople, J. Am. Chem. Soc. **97**, 3402 (1975).

[46] S. S. Han, A. C. T. van Duin, W. A. Goddard III, and H. M. Lee, J. Phys. Chem. A **109**, 4575 (2005).

[47] B. B. Iversen, F. K. Larsen, M. Souhassou, and M. Takata, Acta. Cryst. B **B51**, 580 (1995).

[48] M. Y. Chou, P. K. Lam, and M. L. Cohen, Phys. Rev. B **28**, 4179 (1983).

[49] P. Blaha and K. Schwarz, J. Phys. F: Met. Phys. **17**, 899 (1987).

[50] M. H. McAdon and W. A. Goddard III, Phys. Rev. Lett. **55**, 2563 (1985).

[51] M. Li and W. A. Goddard III, J. Chem. Phys. **98**, 7995 (1993).

[52] E. Wigner, Phys. Rev. **46**, 1002 (1934).

[53] D. M. Ceperley and B. J. Alder, Phys. Rev. Lett. **45**, 566 (1980).

[54] J. P. Perdew and Y. Wang, Phys. Rev. B **45**, 13244 (1992).

[55] D. G. Hicks, T. R. Boehly, P. M. Celliers, J. H. Eggert, S. J. Moon, D. D. Meyerhofer, and G. W. Collins, Phys. Rev. B **79**, 014112 (2009).

[56] H. M. Van Horn, Science **252**, 384 (1991).

[57] M. K. Matzen, M. A. Sweeney, R. G. Adams, J. R. Asay, J. E. Bailey, G. R. Bennett, D. E. Bliss, D. D. Bloomquist, T. A. Brunner, R. B. Campbell, G. A. Chandler, C. A. Coverdale, M. E. Cuneo, J.-P. Davis, C. Deeney, M. P. Desjarlais, G. L. Donovan, C. J. Garasi, T. A. Haill, C. A. Hall, D. L. Hanson, M. J. Hurst, B. Jones, M. D. Knudson, R. J. Leeper, R. W. Lemke, M. G. Mazarakis, D. H. McDaniel, T. A. Mehlhorn, T. J. Nash, C. L. Olson, J. L. Porter, P. K. Rambo, S. E. Rosenthal, G. A. Rochau, L. E. Ruggles, C. L. Ruiz, T. W. L. Sanford, J. F. Seamen, D. B. Sinars, S. A. Slutz, I. C. Smith, K. W. Struve, W. A. Stygar, R. A. Vesey, E. A. Weinbrecht, D. F. Wenger, and E. P. Yu, Phys. Plasmas **12**, 055503 (2005).

[58] W. J. Nellis, S. T. Weir, and A. C. Mitchell, Phys. Rev. B **59**, 3434 (1999).

[59] D. Saumon, G. Chabrier, and H. M. Van Horn, Astrophys. J. **99**, 713 (1995).

[60] P. Loubeyre, R. LeToullec, D. Hausermann, M. Hanfland, R. J. Hemley, H. K. Mao, and L. W. Finger, Nature (London) **383**, 702 (1996).

[61] C. Narayana, H. Luo, J. Orloff, and A. L. Ruoff, Nature (London) **393**, 46 (1998).

[62] W. J. Nellis, A. C. Mitchell, M. van Thiel, G. J. Devine, R. J. Trainor, and N. Brown, J. Chem. Phys. **79**, 1480 (1983).

[63] M. D. Knudson, D. L. Hanson, J. E. Bailey, C. A. Hall, and J. R. Asay, Phys. Rev. Lett. **90**, 035505 (2003).

[64] G. V. Boriskov, A. I. Bykov, R. I. Ilkaev, V. D. Selemir, G. V. Simakov, R. F. Trunin, V. D. Urlin, A. N. Shuikin, and W. J. Nellis, Phys. Rev. B **71**, 092104 (2005).

[65] B. Militzer, Ph.D. thesis, University of Illinois at UC, 2002.

[66] B. Militzer and D. M. Ceperley, Phys. Rev. E **63**, 066404 (2001).

[67] B. Militzer and D. M. Ceperley, Phys. Rev. Lett. **85**, 1890 (2000).

[68] P. M. Celliers, G. W. Collins, L. B. Da Silva, D. M. Gold, R. Cauble, R. J. Wallace, M. E. Foord, and B. A. Hammel, Phys. Rev. Lett. **84**, 5564 (2000).

[69] M. Thompson, M. D. Baker, A. Christie, and J. F. Tyson, *Auger Electron Spectroscopy* (Wiley, New York, 1985).

[70] M. L. Knotek and P. J. Feibelman, Phys. Rev. Lett. **40**, 964 (1978).

[71] D. E. Ramaker, Springer Ser. Chem. Phys. **24**, 70 (1983).

[72] H. P. Gillis, D. A. Choutov, J. D. Piper, J. H. Crouch, P. M. Dove, and K. P. Martin, Appl. Phys. Lett. **66**, 2475 (1995).

[73] H. P. Gillis, D. A. Choutov, K. P. Martin, and L. Song, Appl. Phys. Lett. **68**, 2255 (1996).

[74] J. Zemek, J. Potmesil, M. Vanecek, B. Lesiak, and A. Jablonski, Appl. Phys. Lett. **87**, 262114 (2005).

[75] A. Hoffman and A. Laikhtman, J. Phys.: Condens. Matter **18**, S1517 (2006).